Climatology of the Heat Low and the Intertropical Discontinuity in the Arabian Peninsula

Ricardo Fonseca[1], Diana Francis[1], Narendra Nelli[1], and Mohan Thota[2]

[1]Khalifa University
[2]NCMWF

November 23, 2022

Abstract

In this paper, the climatological state and the seasonal variability of the Arabian Heat Low (AHL) and the Intertropical Discontinuity (ITD) are investigated over the Arabian Peninsula using the 1979-2019 ERA-5 reanalysis data. The AHL is a summertime feature, mostly at 15º-35ºN and 40º-60ºE, exhibiting a clear strengthening over the last four decades in line with the observed increase in surface temperature. However, no clear shift in its position is detected. The AHL, driven by both thermodynamic and dynamic forcing, is broader and stronger during daytime, and exhibits considerable variability on day-to-day time-scales, likely due to the convection associated with the Asian summer monsoon. The ITD is the boundary between the hot and dry desert air and the cooler and more moist air from the Arabian Sea. It lies along the Arabian Peninsula's southern coastline in the cold season but reaches up to 28º N between 50º - 60º E in the summer months. While in the former it has a rather small diurnal variability, in the latter it shows daily fluctuations of up to 10º in latitude. The presence of the Sarawat Mountains over southwestern Saudi Arabia preclude a northward migration of the ITD in this area. The ITD exhibited a weak northward migration in the 41-year period, likely due to the increased sea surface temperatures in the Arabian Sea. On inter-annual timescales, the El Niño-Southern Oscillation, the Indian Ocean Dipole, and solar-geomagnetic effects play an important role in the AHL's and ITD's variability.

Climatology of the Heat Low and the Intertropical Discontinuity in the Arabian Peninsula

Ricardo Fonseca[1], Diana Francis[1*], Narendra Nelli[1], Mohan Thota[2]

[1] Khalifa University of Science and Technology, P. O. Box 54224, Abu Dhabi, United Arab Emirates.

[2] National Centre for Medium Range Weather Forecasting, Ministry of Earth Sciences, Noida, India.

***Corresponding Author:** *Dr. Diana Francis, diana.francis@ku.ac.ae*

Abstract:

In this paper, the climatological state and the seasonal variability of the Arabian Heat Low (AHL) and the Intertropical Discontinuity (ITD) are investigated over the Arabian Peninsula using the 1979-2019 ERA-5 reanalysis data. The AHL is a summertime feature, mostly at 15º-35ºN and 40º-60ºE, exhibiting a clear strengthening over the last four decades in line with the observed increase in surface temperature. However, no clear shift in its position is detected. The AHL, driven by both thermodynamic and dynamic forcing, is broader and stronger during daytime, and exhibits considerable variability on day-to-day time-scales, likely due to the convection associated with the Asian summer monsoon. The ITD is the boundary between the hot and dry desert air and the cooler and more moist air from the Arabian Sea. It lies along the Arabian Peninsula's southern coastline in the cold season but reaches up to 28º N between 50º - 60º E in the summer months. While in the former it has a rather small diurnal variability, in the latter it shows daily fluctuations of up to 10º in latitude. The presence of the Sarawat Mountains over southwestern Saudi Arabia preclude a northward migration of the ITD in this area. The ITD exhibited a weak northward migration in the 41-year period, likely due to the increased sea surface temperatures in the Arabian Sea. On inter-annual timescales, the El Niño-Southern Oscillation, the Indian Ocean Dipole, and solar-geomagnetic effects play an important role in the AHL's and ITD's variability.

Keywords: Heat Low, Convergence zone, Intertropical Front, Monsoon system, Arid regions, Land-Sea interactions.

1. Introduction

Thermal heat lows and convergence zones between moist and dry air masses are ubiquitous features of tropical and subtropical regions (i.e., Flamant *et al.*, 2007, Dumka *et al.*, 2019). They play a crucial role in modulating the mesoscale meteorological features in these regions, such as the mesoscale convection, dust storms and monsoon surge and associated rain (e.g., Bou Karam *et al.*, 2014). Like the other deserts regions, the Arabian Peninsula witnesses the development of a thermal heat low during the summer season and consequently the inland advance of the intertropical front or the Intertropical Discontinuity (ITD), located over the Arabian Sea during the winter season. In this study, we aim at characterizing these two features over the Arabian Peninsula and establishing the knowledge on their seasonal and inter-annual variability.

The Arabian Desert, a vast arid region located in the Middle East that extends over 2.33×10^6 km^2, is one of the driest places on Earth (Cosnefroy *et al.*, 1996). The majority of the meager and irregular precipitation falls in the cold season, in association with mid-latitude baroclinic systems (e.g. Niranjan Kumar and Ouarda, 2014; Al Senafi and Anis, 2015; Wehbe *et al.*, 2018). Summertime rainfall is mostly confined to the southern part of the Arabian Peninsula in association with the Asian summer monsoon (Babu *et al.*, 2016), where localized convective events form during summer (Steinhoff *et al.*, 2018; Branch *et al.*, 2020; Wehbe *et al.*, 2020). As a result of the strong heating of the surface by the Sun, a thermal low, hereafter denoted as the Arabian Heat Low (AHL), develops, with a well-mixed layer from the surface up to 650 hPa during mid-afternoon hours (e.g. Blake *et al.*, 1983). While ascent prevails in the lowest 1 km above ground level (AGL), at all levels above 1 km there is a descending motion, associated with the downward branch of the Hadley circulation and Asian summer monsoon (Steinhoff *et al.*, 2018). The AHL is a shallow, cyclonic, warm-core low-pressure system in the lowest kilometer of the atmosphere (e.g., Racz and Smith 1990). A more comprehensive investigation of the structure of the AHL is given in Smith et al. (1986a, b), using satellite, aircraft and surface data from field experiments conducted in the warm season of 1979-1982. A swing of about 50ºC in the 2 cm deep temperature at a weather station in the Arabian Desert between day and night is observed, with the surface energy budget, in a daily averaged sense, dominated by a balance between the sensible heat flux and the net radiation flux. The latter has also been reported by Nelli *et al.* (2020a), in an analysis of eddy-covariance measurements at Al Ain in the United Arab Emirates (UAE). The interaction between the AHL and the southwest Asian monsoon is found to be two-way: the monsoon helps to maintain the heat low through large-scale descent and adiabatic warming, while the thermal advection into the western Arabian Sea confines the low-level moisture within the monsoon low-level jet, aiding in its sustenance (Ackerman and Cox, 1982). On intra-seasonal timescales, the two systems are also intertwined. As noted by Steinhoff *et al.* (2018), active phases of the Asian summer monsoon are associated with enhanced upward motion and convection over the Arabian Sea, with the resulting anomalous subsidence over the Arabian Peninsula leading to a stronger AHL. The AHL also plays an important role in modulating the occurrence of convection. An intense AHL over land during the day, drags maritime air masses inland and enhances low-level convergence, which is essential for cloud formation in this region (Francis *et al.*, 2021; Schwitalla *et al.*, 2020).

Convergence lines are of the utmost importance in meteorology, given their role in convection initiation and subsequent occurrence of precipitation (e.g. Weller *et al.*, 2019; Branch *et al.*, 2020). A well-known convergence line in the tropics and subtropics is the ITD, where the hot and dry desert air converges with the cooler and moist tropical maritime air somewhere in the 0-30º latitude band (Bou Karam *et al.*, 2008; Pospichal *et al.*, 2010). This interface marks the leading edge of the monsoon flow, and is often mixed with the Intertropical Convergence Zone (ITCZ), even though the two features are clearly distinct, as noted by Williams (2008). The ITCZ generally lies some 500 km south of the ITD (Hamilton and Archibald, 1945; Lélé and Lamb, 2007), and represents the core region of tropical convection. The ITD separates the moist monsoon layer to the south from the dry boundary layer to the north (Williams, 2008).

Several studies have been conducted over Africa on the variability and dynamical role of the ITD. For example, Bou Karam *et al.* (2008) characterized the ITD using airborne measurements and highlighted the importance of the ITD in lifting and subsequent transport of dust over the Sahara. Furthermore, the combination of the ITD and the presence of orography can lead to dry cyclogenesis and subsequent dust emissions over the Sahel (Bou Karam *et al.*, 2009b). The role of the ITD on dust activities has also been noted by e.g. Knippertz (2008) and Lyngsie *et al.* (2013), and more recently by Francis *et al.* (2020a) on its contribution to the historical dust storm of June 2020 that extended into the tropical Atlantic Ocean and North America.

Odekunle (2010) and Odekunle and Adejuwon (2017) reported on the effects of the ITD on the variability of the precipitation regimes in Nigeria. While on seasonal scales it follows the annual march of the Sun, over a diurnal cycle the ITD position can fluctuate by 1º- 2º, northwards during the night and southwards during the day, in line with the diurnal cycle of the PBL (Lothon *et al.*, 2008), and the expansion of the thermal low during the day (Sultan *et al.*, 2007). Elsewhere, there are very few studies on the dynamics of the ITD. Rashki *et al.* (2019) found that it plays an important role in the dust variability over the Arabian Sea, with the convergence of the northwesterly (Shamal) winds, southwesterly (monsoon) winds, and northerly (Levar) winds leading to the accumulation of large amounts of dust aerosols over northern and central parts of the Arabian Sea in the summer. Dumka *et al.* (2019) characterized the ITD over northern India and stressed the role it played in dust lifting and vertical transport. Both studies focused on an individual period during a summer month, and do not explore how the ITD fluctuates in the region throughout the year, nor on its inter-annual variability.

Despite being key elements of the regional climate and weather patterns, the characteristics of the thermal low and the ITD, as well as their spatio-temporal variability over the Arabian Peninsula, have not been established yet. The aim of this work is to investigate the mean state and variability of the AHL and ITD on different timescales, an important step given their wide-range implications for weather and climate processes. While a similar analysis has been conducted in the neighboring Sahara Desert (e.g. Lothon *et al.*, 2008; Lavaysse *et al.*, 2009; Pospichal *et al.*, 2010), to the best of the authors' knowledge, it has not been performed over the Arabian Peninsula and adjacent regions.

This paper is structured as follows. In section 2, the methodologies used to detect the thermal low and the ITD, as well as the set-up of the numerical model used to test some of the hypotheses put forward in the analysis of the reanalysis data, are described. The discussion of the spatio-temporal variability of the AHL and ITD is then presented in sections 3 and 4, respectively, while in section 5, the main findings are summarized.

2. Methodology

In this section, the most commonly used measures to identify a heat low and the ITD are outlined. They have been employed in the Arabian Peninsula using ERA-5 reanalysis data (Hersbach *et al.*, 2020), extending from 1979 to 2019. ERA-5 was selected due to its higher spatial (0.25º or ~27 km) and temporal (hourly) resolution when compared to other commonly used reanalysis datasets such as ERA-Interim and the Climate Forecast System Reanalysis (e.g. see Table 2 of Francis *et al.*, 2021), and its overall good performance over this region. The latter can be seen in Figs. 1b-d, where the ERA-5 predictions at the closest grid-point to the location of three airports in the region are compared with the observed values for a one-week period in July 2018. The slight offset in the mean sea-level pressure at station #1 and, in particular, at station #3, is due differences in the terrain, which at ~27 km resolution is not fully captured by ERA-5.

2.1. Thermal Low detection

To detect the AHL, we consider the same metrics implemented by previous studies to identify and characterize the Sahara Heat Low (SHL), the AHL's counterpart over the Sahara Desert, for which several measures have been employed in published works. For example, Lavaysse *et al.* *(*2009) used the low-level atmospheric thickness (LLAT) criterion to detect the SHL. The LLAT is the 700-925 hPa geopotential height thickness, with the SHL corresponding to the region with the 10% highest LLAT in the domain 20ºW-30ºE and 0º-40ºN. A similar approach was followed by Engelstaedter *et al.* (2015) and Wang *et al.* (2015). The idea is that the presence of the SHL and associated low-level temperature-increase leads to an expansion of the lower atmosphere, and therefore higher LLATs. Chauvin *et al.* (2010) used the maximum in the 850 hPa potential temperature, $\theta_{850\ hPa}$, a level located at roughly 3000 m AGL, to characterize the SHL. This field is correlated with the LLAT (Roehrig *et al.*, 2011). Flamant *et al.* (2007) identified the SHL using the 1006 hPa threshold of the mean sea-level pressure. Here we use all the three metrics described above over the domain 10º-35ºN and 40º-60ºE for 03 UTC. As explained in Lavaysse *et al.* (2009), the detection of the SHL is conducted just before local sunrise, at 06 UTC in west Africa, as at this time the low-level temperature field is least affected by the presence of clouds and the complex surface albedo pattern. As west Africa is roughly three time zones behind the Arabian Peninsula, the choice of 03 UTC is justified. In addition to the referred metrics, the relative vorticity at 850 hPa, $\xi_{850\ hPa}$, used by Steinhoff et al. (2018) in their study of a convective event over western UAE in late August 2011, is also considered.

In order to assess the performance of the different metrics, Fig. 2 shows them on a single day (11 July 2018) at 00, 06, 12 and 18 UTC (similar conclusions are reached for other days, not shown). The first panel gives the LLAT in shading, while the stipple shows the AHL using the LLAT metric proposed by Lavaysse *et al.* (2009). In order to construct this plot, and for a given time stamp, the cumulative distribution of the LLAT for the domain 10ºN-35ºN and 40ºE-60ºE, which encompasses the Arabian Peninsula where the AHL develops, is first generated. As the geopotential height is extrapolated below orography in the reanalysis dataset, all regions for which the 925 hPa pressure level is below the surface are excluded from the analysis. In addition, the water bodies are also masked out, as the thermal low is, by definition, a land-based feature. The top 10% of the values are then plotted. The second to fourth panels show $\theta_{850\ hPa}$, sea level pressure, and $\xi_{850\ hPa}$, with the AHL region also stippled. In all panels, the 2-meter temperature equal to 40ºC isotherm is drawn as a solid contour, so as to highlight the warmest regions at a given time.

The AHL extends over a broad region around the Arabian Gulf. Spatially, it is not only more intense during daytime, but also broader, as a result of the strong surface heating. At night, and in particular around local sunrise (06 UTC) when it is defined following Lavaysse *et al.* (2009), the AHL largely coincides with the region where $\theta_{850\ hPa}$ is the highest and the sea-level pressure is the lowest, in line with theoretical arguments (e.g. Blake *et al.*, 1983; Smith 1986a, b; Rácz and Smith, 1999). However, during daytime and evening hours, the heat low in the pressure field is centered over southeastern Saudia Arabia, where the air temperature is higher and a cyclonic circulation at 850 hPa is present. The AHL defined using the LLAT metric only includes the northern part of the core of the referred low pressure, whose signature is also not present in the $\theta_{850\ hPa}$ plot. This is a drawback of using the LLAT to identify the thermal low during daytime, even though it is important to note that, as stated before, the definition used here was designed for nighttime hours and just before sunrise.

The $\xi_{850\ hPa}$ field also appears to be a good metric to diagnose the thermal low but only on a daily basis, as no signature of the heat low using this metric is detected in the climatological analysis as it will be shown later. Fig. 2 shows a region of low-level cyclonic vorticity over southeastern Saudi Arabia to the south of the UAE at all times, with a higher amplitude of about 10^{-4} s^{-1} at 06 UTC in line with Rácz and Smith (1999), and only partially captured by the AHL using the LLAT definition. The low-level convergence on 11 July 2018 is broadly in the same area (although the peak region is further north) to the one on 30 August 2011 shown in Steinhoff *et al.* (2018), their Fig. 2. The vortex is slightly displaced with respect to the minimum in the sea-level pressure, which is indicative of a baroclinic signature in line with expectations (e.g. Smith 1986a and b), and is of a smaller spatial extent. What is more, no clear signal is present in that region in the LLAT field, with a relative minimum shown in the $\theta_{850\ hPa}$ plot. An inspection of the vertical velocity at 850 hPa indicates stronger ascent in the area where $\theta_{850\ hPa}$ is lower (not shown), suggesting that the near-surface potential temperature here is reduced when compared to neighbouring regions, likely due to stronger radiative cooling at this more inland site.

In summary, the AHL defined using the LLAT field is able to diagnose the thermal low mostly at night and just before sunrise, with the defined AHL largely coinciding with the areas where $\theta_{850\ hPa}$ is the highest and the sea-level pressure is the lowest, in line with Smith (1986a, b). During daytime, however, when it is broader and has a larger magnitude, the LLAT is not as good of a metric to identify it, with the sea-level pressure or $\xi_{850\ hPa}$ preferred. As the AHL is defined around 00-06 UTC, the LLAT definition will be used in the subsequent discussion.

2.2. Intertropical Discontinuity detection

As the boundary between the hot and dry desert air and the cooler and moist marine air, the ITD has been widely defined using the 2-meter dew-point temperature. For example, Buckle (1996), Bou Karam *et al.* (2009a), Flamant *et al.* (2009) and Chaboureau *et al.* (2016) used a value of 14ºC for this purpose, while Grams *et al.* (2010), and Lafore *et al.* (2017) considered 15ºC. Lothon *et al.* (2008) and Kalapureddy *et al.* (2010) identified the ITD as the line of maximum horizontal gradient of the dew-point temperature. Bou Karam *et al.* (2009b) defined the ITD as the region of maximum meridional gradient of the integrated water vapour content, focusing on the moisture contrast across the interface. In addition to moisture-based diagnostics, some authors have considered the wind reversal associated with the ITD to detect it. For example, Flamant *et al.* (2007) and Pospichal *et al.* (2010) defined the ITD as the latitude of the reversal of the 925 hPa wind field from southerly to the northerly along the interface, a similar approach to that followed by Bou Karam *et al.* (2008). Lavaysse *et al.* (2009) also looked into the wind reversal but by finding the minimum in the 925 hPa geopotential height between the equator and 28ºN. Odekunle *et al.* (2010) used a combination of the two criteria above (i.e. surface wind convergence and a dew-point temperature threshold of 15ºC), together with the discontinuities in dry bulb temperature and surface pressure. The ITD is usually defined at night, when it is most stable and not affected by the presence of the daytime thermal convection (Lothon *et al.*, 2008). In a study over the Arabian Sea, Rashki *et al.* (2019) identifies the ITD as the region of zero meridional wind at 850 hPa, while Dumka *et al.* (2019) over India defines it as the area of weak winds of less than 4 m s^{-1} at 925 hPa, where two opposing wind regions converge. For the 925 hPa pressure level, considered in the vast majority of the studies above to detect the ITD, using the reversal of the wind direction to identify this feature gives similar results to employing the dew-point temperature criterion with a threshold of 15ºC at 00 UTC (not shown). Given this, the dew-point criterion, with a threshold of 15ºC applied over the domain 13ºN-38ºN and 43ºE-70ºE at 00 UTC, is considered due to its added simplicity.

2.3. Numerical Simulations

In order to better understand the role of the orography on the ITD, simulations with the Weather Research and Forecasting (WRF; Skamarok *et al.*, 2008) model are also conducted. Two runs are performed: a real-case, where WRF is run as per normal, and a semi-idealised run, where the orography is removed. The period targeted for the modelling work is 11-18 July 2018. The run is initialized on 10 July, with the first day regarded as spin-up and its output discarded. WRF is run with a single nest at 12 km spatial resolution, with the domain comprising the whole of the Middle East and surrounding region, as shown in Fig. 1. The model configuration, listed in Table 1, is as in Francis *et al.* (2021), which has been found to work well for warm season simulations in this region.

A comparison between the WRF predictions and the observed measurements at the three sites, given in Figs. 1b-d, shows a clear cold bias, more pronounced in the evening and nighttime hours. This is a well-known model bias, reported e.g. in Weston *et al.* (2018), Nelli *et al.* (2020b), Schwitalla et al. (2020) and Temimi *et al.* (2020), that is also seen in other arid regions such as the Sahara desert (e.g. Fekih and Mohamed, 2019). It has been attributed to deficiencies in the physics schemes, in particular in the Land Surface Model (LSM) and radiation scheme, and/or an incorrect representation of the surface properties and concentration of atmospheric gases and dust. Using a different planetary boundary layer parameterization scheme (Chaouch *et al.*, 2017), tweaking tunable parameters inside the LSM (Weston *et al.*, 2018) and surface layer (Nelli *et al.*, 2020b) schemes, or employing a more realistic representation of the soil texture and land use land cover (Temimi *et al.*, 2020), does not seem to alleviate this problem. A correction of the WRF cold bias is beyond the scope of this work. Despite these biases, however, the WRF model gives a good representation of the AHL and atmospheric fields such as sea-level pressure, and low-level potential temperature and relative vorticity. This can be seen by comparing Fig. S1 with Fig. 2. The cold bias can be seen as the 2-meter temperature contour covers a much-reduced area in Fig. S1 when compared to Fig. 2, where ERA-5 data, which is more accurate as seen in Figs. 1b-d, is used. However, the WRF-predicted AHL is not that different from that predicted by ERA-5, with the minimum in sea-level pressure and the cyclonic vortex in $\xi_{850\ hPa}$ being roughly in the same place, and having a comparable magnitude, to the correspondent ones in the reanalysis plot. This highlights the potential use of the WRF model to investigate further this feature, at least on a day-to-day basis. Having said that, in this study the model will only be employed to investigate the role of the topography on the position of the ITD by comparing the output of a real-case to that of a semi-idealised simulation. The bulk of the analysis conducted here only makes use of the reanalysis dataset.

3. The Arabian Heat Low

As summarized in section 2.1, LLAT, $\theta_{850\ hPa}$, sea-level pressure and $\xi_{850\ hPa}$ diagnostics have been used to detect heat lows. Here, the analysis will be extended to monthly mean fields averaged over the 41-year (1979-2019) ERA-5 data, with the results given in Fig. 3 at 03 UTC (07 LT), just before or around local sunrise.

3.1 Spatial Extent and Annual Cycle

The AHL is found to be exclusively a summer feature, only present from June to September (JJAS), and hence the fields are only shown in the warmer months. The AHL achieves its highest amplitude in July, when the surface/air temperatures in the region peak (e.g. Al Senafi and Anis, 2015; Branch *et al.*, 2020; Nelli *et al.*, 2020a). It covers a broad region, extending from the Rub' Al Khali desert in central Saudi Arabia to the shores of the Arabian Gulf and Sea of Oman. It also comprises some of the valleys in Iran. Indeed, the AHL is part of the Asian summer monsoon trough, which has a rather broad spatial extent (e.g. Yu *et al.*, 2016). The solid blue line corresponds to the 2-meter temperature equal to 40ºC contour, and it largely overlaps with the AHL, as expected from theoretical considerations (e.g. Smith 1986a and b). On top of the thermodynamic forcing, the AHL is also partially dynamically driven. Fig. 4a gives the vertical velocity and horizontal winds at 850 hPa for the same months and time of the day. It shows a broad region of low-level convergence and ascent over central Saudi Arabia, where the northwesterly turning northeasterlies (Shamal) winds slow down, and also converge with the southwesterly (monsoon) winds. This region of upward motion roughly matches the area where the highest $\theta_{850\ hPa}$ are seen, Fig. 3b, and is also part of the AHL obtained with the LLAT criterion.

The similarity between the LLAT and $\theta_{850\ hPa}$ has been noted e.g. by Roehrig *et al.* (2011), even though for the Arabian Peninsula in the summer months, the latter is dominated by the dynamic forcing. Conversely, the sea-level pressure field, Fig. 3c, picks up more of the thermodynamic forcing, with the AHL encompassing the regions of lowest sea-level pressures. The fact that the near-surface low lies in regions of low topography is consistent with the findings of Lavaysse *et al.* (2009, 2013), whom reported that low-elevation regions are preferred sites for thermal lows. As opposed to the LLAT, $\theta_{850\ hPa}$ and sea-level pressure fields, and to the conclusions reached in the analysis of the 1-day event in Fig. 2, however, the vorticity field, $\xi_{850\ hPa}$, given in Fig. 3d, does not seem to properly capture the signature of the AHL. The areas of low-level convergence are rather weak and small in size, with this field being dominated by negative values that arise from the presence of the subtropical anticyclone (Spinks et al., 2015). This is expected, as $\xi_{850\ hPa}$ is a noisy field, with a great deal of cancellation taking place when doing long-term averages. Low-level convergence is primarily confined to regions of complex topography, such as southern and western parts of Yemen, and the high-terrain over Zagros Mountains and the Hindu

Kush. A comparison with the annual cycle of the SHL, given in Fig. 4 of Lavaysse *et al.* (2009), reveals that the AHL has a more intricate structure, owing to the more complex topography and land-sea patterns of the Arabian Peninsula.

3.2 Diurnal Variability

In order to investigate the diurnal variability of the AHL, the spatially-averaged LLAT over the AHL region, regarded as the AHL index, is plotted for the June to September months in Fig. 4b. The lowest LLAT occurs around 05-06 UTC (09-10 LT) and the highest around 14 UTC (18 LT), roughly two hours after the surface and air temperatures in the region reach their extrema (e.g. Nelli *et al.*, 2020a). This lag arises from the fact that it takes time for the sensible heat fluxes to warm up the lower-levels of the atmosphere. The phase of the diurnal cycle is robust throughout the warm season, with the higher thicknesses in July consistent with the observed temperature annual cycle (e.g. Al Senafi and Anis, 2015; Branch *et al.*, 2020; Nelli *et al.*, 2020a). Figs. 4c-d are as Fig. 4b but for $\theta_{850\ hPa}$ and sea-level pressure, respectively. They show a similar monthly variability and phase of the diurnal cycle as the LLAT. The double minima, at about 14 UTC (18 LT) and 23 UTC (03 LT), and maxima, at roughly 06 UTC (10 LT) and 19 UTC (23 LT), seen in the pressure field also arises from the atmospheric tides (Nelli *et al.*, 2020a).

3.3 Intra-Seasonal Variability

On top of the diurnal variability, the AHL also exhibits considerable intra-seasonal variability. This can be seen in Fig. 5a, which shows the hourly AHL index from May to September 2018. In order to obtain this index, and for a given time-stamp, we first compute the AHL based on the proposed LLAT metric discussed in section 2.1. Then, we take the averaged LLAT over the AHL region, a measure of its strength. The averaged latitude and longitude of the AHL region, which give information regarding its spatial variability, are plotted in Fig. 5b.

Intra-seasonal variability in the strength and spatial extent of a thermal low has been reported in arid regions such as the Sahara Desert. For example, Wang *et al.* (2017) noted a 10-day cycle in the Saharan heat low, where it first built up over the core of the desert, migrated westwards over the following 3-5 days, and finally collapsed around the west African coastline. The westward migration may be related to (i) warm and dry air advection from the north to the west of system in association with the cyclonic circulation; (ii) cold and moist air along its eastern edge due to convective systems; (iii) propagation of mid-latitude Rossby waves along the North Atlantic - North African waveguide. The collapse of the heat low around the coast is due to cold and humid air advection, in association with a cold oceanic current that flows near the coastline (e.g. Parker and Diop-Kane, 2017). Day-to-day variability has also been reported for the AHL, such as in Ackerman and Cox (1982) and Steinhoff *et al.* (2018), and is found to be linked with the Asian summer monsoon.

An inspection of Fig. 5a reveals a variability of the AHL on time-scales of about 5-15 days. A comparison with Fig. 5b suggests that, a north-westward migration of the AHL, i.e. towards the core of the Arabian Desert, is typically accompanied by its intensification, while a movement to the southeast, i.e. closer to the Arabian Sea, sees its weakening, a behaviour consistent with that of the SHL described in Wang *et al.* (2017). In order to illustrate the two extreme states, Figs. 5c and 5d show the LLAT, AHL, and 10-meter horizontal winds at 03 UTC on 07 and 16 June 2018, respectively, roughly when the index reaches its highest and lowest value for the summer of 2018.

The two snapshots reveal a remarkable contrast in the spatial extent and magnitude of the thermal low: while on 07 June, the LLAT exceeds 2450 m over the bulk of the AHL region, on 16 June it dropped up to 50 m in that region, with the AHL found further south, over Oman and northern Yemen. In addition, the northwesterly (Shamal) winds are stronger over the Gulf on 16 June, and advect the lower thicknesses over Iraq/Kuwait southeastwards. The higher magnitude wind speeds are consistent with a deeper and broader monsoon trough on 16 June (not shown), which gives rise to a steeper pressure gradient with respect to the subtropical high (Yu *et al.*, 2016). As the monsoon trough is closely related to the Indian Summer Monsoon, this suggests that summertime weather conditions in the Arabian Peninsula are linked with the intra-seasonal variability of the Indian Summer Monsoon. This connection is well known, and has been explored e.g. by Steinhoff *et al.* (2018) and Attada *et al.* (2019). In a nutshell, enhanced convective activity, and therefore ascent, over the Arabian Sea and Indian subcontinent leads to stronger descent over the Arabian Peninsula, and subsequently a deeper thermal low, which in turn strengthens the lower-level winds. As a result of increased moisture advection from the surrounding seas, summertime convection over western UAE is more frequent during the decay phase of the AHL, as noted by Steinhoff *et al.* (2018).

In addition to the referred intra-seasonal variability, it is interesting to note in Fig. 5a the sudden build-up of the AHL from late May to early June, accompanied by a north-eastward migration, Fig. 5b, and its rapid decline in September, associated with a south-westward movement. This is reminiscent of what has been reported over the Sahara desert (e.g. Redelsperger *et al.*, 2002; Sultan and Janicot, 2003). Besides the annual march of the Sun, this may arise from the fact that the majority of the precipitation in the region occurs in winter and early spring (e.g. Nelli *et al.*, 2020a). Once the soil (and the atmosphere) is bone dry, the heat low can develop very quickly.

3.4 Inter-annual Variability and Climatological Trends

Fig. 6a shows the June to September (JJAS)-averaged AHL index over the 41 year-period. The AHL exhibits a clear positive trend, which is statistically significant at the 95% confidence level, with the LLAT increasing at a rate of about 0.2 m/year, giving a relative increase of roughly 0.3% over a 40-year period. This is not surprising, as several studies have highlighted the increase in surface/air temperature in the region over the last few decades (e.g. Almazroui *et al.*, 2014), which is also seen in the ERA-5 data (Fig. 6b) and is also statistically significant at the 95% confidence level. It is also interesting to note that, while the surface temperature in the AHL domain (10º-35ºN, 40º-60ºN) but outside the AHL region has been increasing over the last four decades (Fig. 6c), the rate of increase is roughly 35% lower and the temperatures about 2 K less than in the AHL region. In other words, while the warming tendency is not confined to the AHL, it is more pronounced in the heat low region. Further analysis of the surface temperature variability in the region, including the land-sea temperature gradient, is outside the scope of this study.

There is considerable inter-annual variability in the AHL index, with anomalously high values in 1998 and 2017, and low values in 1992, 2004 and 2013. As the summers of 1998 and 2017 featured a La Nina and those of 1992 and 2004 an El Nino (2013 was a neutral summer), it appears that the El Nino-Southern Oscillation (ENSO; Huang *et al.*, 2017) may play an important role in the variability of the AHL. This is confirmed in a wavelet analysis, Fig. 7a, which shows higher power for timescales of 2-4 years, the prevailing timescales of ENSO variability (e.g. Berner *et al.*, 2020). ENSO is known to have a significant impact on the Indian summer monsoon: the enhanced convection over the Maritime Continent in La Nina events, leads to anomalous westerlies over the tropical Indian Ocean, which act to strengthen the monsoon's circulation, a relationship modulated by the Indian Ocean SSTs (e.g. Hrudya *et al.*, 2020; Srivastava *et al.*, 2020). At the same time, and as highlighted before, enhanced convection over the Indian subcontinent and Arabian Sea leads to anomalous descent over the Arabian Peninsula, and hence to an intensification of the AHL. In addition to ENSO, the Indian Ocean Dipole (IOD; Saji *et al.*, 1999) also has a peak in that region of the spectrum (Wang *et al.*, 2019), and may impact the AHL through changes in the convection in the Arabian Sea. In particular, positive IOD events are accompanied by higher than average SSTs over the western Indian Ocean, which will increase the likelihood of convective activity over the Arabian Sea, and subsequently descent and adiabatic warming over the Arabian Peninsula. The higher power around a time-scale of 2 years may be linked to the biennial oscillation in the Asian-Australian monsoon system, connected to both ENSO and IOD (e.g. Konda *et al.*, 2018). In addition to the referred modes of variability, increased solar activity and the resulting stronger surface heating are also likely to strengthen the AHL (e.g. Misios *et al.*, 2016).

In order to better visualize the change in the AHL's magnitude and spatial extent with time, Fig. 8a and Fig. 8b show Hovmoller plots averaged over 40ºE-60ºE and 15ºN-25ºN, respectively, where the bulk of the thermal low is found (Fig. 3). Here, the LLAT anomalies with respect to the 1979-2019 monthly climatology normalized by its standard deviation are plotted. A positive trend is seen, with negative values prevailing before 1997-1998, and positive values since then. The transition, which takes place around 1997-1998, is likely linked with a change in the dominant phase of ENSO and associated teleconnections. As reported by Niranjan Kumar and Ouarda (2014) and Aldababseh and Temimi (2017), El Nino events were more frequent from the late 1970s to the mid-1990s, while La Nina events have occurred more often from mid-1990s. Figs. 8a and 8b do not show any significant shift in the position of the AHL over the 41 year-period, with the largest anomalies seen around 15-25ºN and 40-50ºE, in the western half of the AHL.

4. The Intertropical Discontinuity

4.1 Spatial Extent and Annual Cycle

Being the interface between hot and dry northerly winds and the cooler and moist southerly winds, both moisture-based and wind-based diagnostics have been employed to detect the ITD (e.g. Pospichal *et al.*, 2010; Lafore *et al.*, 2017). Fig. 9a shows the monthly-mean 2-meter dew-point temperature at 00 UTC with the 10-meter horizontal wind vector superimposed. The near-surface atmospheric circulation in the Arabian Sea features northeasterly winds in the cold season, and southwesterly winds in the warm season, in association with the Asian monsoon (Schott *et al.*, 2009). The background flow over the Arabian Gulf, on the other hand, is from the northwest, stronger in the warm season in response to a more vigorous pressure gradient between the subtropical high over Africa and the western Arabian Peninsula and the Asian summer monsoon trough (Al Senafi and Anis, 2015, Bou Karam *et al.*, 2017). The dew-point temperature is higher in the warm season, reaching or even surpassing 30ºC in the Arabian Gulf and Sea of Oman, as a result of enhanced surface evaporation (Xue and Elthair, 2015).

The ITD, shown by a green colour contour, is along the Saudi Arabian and western Indian coastlines in the cold season, penetrating inland from April to October, up to 28ºN just to the west of 60ºE. In its furthest inland position (July and August), it reaches the southern Iranian coast and the Arabian Gulf, extending into Pakistan. In other words, while the ITD may be of little dynamical interest in the south-western Arabian Peninsula, on its eastern side it is likely to play an important role e.g. in the development of convective events, as a convergence line favours ascent and cloud development (e.g. Francis *et al.*, 2021), and dust episodes (e.g. Rashki *et al.*, 2019). Fig. 9b gives the six-hour diurnal cycle of the ITD. Over the eastern Arabian Peninsula, there is very little diurnal variability in the cold season, but in the warmer months a clear southward shift during daytime and northward shift at night, by as much as 10º, is seen. These daily fluctuations are roughly 5 to 10 times larger than those seen over Africa, and are most probably due to the location of the AHL, which is closer to the nearby seas than the SHL over Africa. The link between the diurnal cycle of the ITD and the daytime expansion of the thermal low has been noted e.g. by Lothon *et al.* (2008) and Lavaysse *et al.* (2010) over Africa. The intensification of the AHL leads to increased moisture advection inland and a northward displacement of the ITD. As the cooler and moist air is advected northward with the ITD, the heat low weakens, and the ITD moves southwards again.

In order to investigate the role of the topography in the position of the ITD, two simulations with the WRF model were performed: a real-case simulation, and a semi-idealised run where all the orography in the model's 12 km domain, Fig. 1, was removed. The WRF predictions on 11 July 2018 at 00 and 12 UTC for both simulations are given in Fig. 10. As in the climatological plots in Fig. 9, the ITD is mostly along the southern Arabian coastline, although it migrates northwards in the eastern side of the peninsula at 00 UTC. In the run without orography, however, the ITD is always inland over the Arabian Peninsula, continuing to exhibit a larger diurnal cycle on the eastern side due to the presence of the Arabian Gulf and subsequent moisture advection by the sea-breeze circulation. The near-surface circulation is also very different in the semi-idealised simulation, with northeasterly winds over the Gulf, in response to a more zonally elongated monsoon low that extends from the UAE and Oman into northern India (not shown), as it is not constrained by the topography. The results of the semi-idealised run highlight the role of the orography in shaping the ITD, and confirm that the coastal position of the ITD over the southwestern Arabian Peninsula is due to the presence of steep topography (Sarawat Mountains) over the site. In particular, the high-terrain over Yemen and parts of Saudi Arabia, where the mountains reach up to 3,666 m above sea-level, blocks the inland progression of the ITD, which is a low-level feature extending up to 2 km in altitude.

4.2 Inter-annual Variability and Climatological Trends

Fig. 11a shows the variability of the summertime ITD position over 40-60ºE. As opposed to the AHL, no marked trend is seen in the data, with a slightly northerly position from 1997-1998 to 2008-2009, even though the overall fluctuation of the median does not exceed 2º. This is confirmed in Fig. 11b, which shows a linear fit to the yearly mean JJAS ITD latitude over the 41-year period. The slope of the line is 0.0164º/year, which corresponds to an overall change in position of roughly 0.7º in 40 years. This weak (but positive and statistically significant at the 95% confidence level) trend likely reflects the increase of the SSTs (and hence surface evaporation) in the Arabian Sea (Kumar *et al.*, 2009), also present in the ERA-5 data (Fig. 6d). In addition, the recent warming of the Arabian Gulf (Fig. 6c) and Sea of Oman (Noori *et al.*, 2019), and subsequent inland moisture advection by the sea-breeze circulation (Eager *et al.*, 2008), may also promote a northerly shift of the ITD position. The wavelet spectrum for the JJAS ITD time-series, presented in Fig. 7b, shows the highest power in the 2-4 and 6-14 year bands. The former is also present in the AHL spectrum, Fig. 7a, and has been attributed to the influence of ENSO and IOD on the atmospheric circulation over the Arabian Peninsula. ENSO is also likely to play a role in the ITD, as the weather conditions in the southern Arabian Peninsula are more humid in La Nina years (Babu *et al.*, 2016), such as in 1983, 1986, 1998 and 2017 (Huang *et al.*, 2017). In addition, the above average SSTs in the western Indian Ocean in positive IOD events will enhance the amount of moisture in the atmosphere through evaporation that is subsequently advected inland (Anil *et al.*, 2016). This may explain the northern migration of the ITD in such episodes. The peak in the 6-14 year band is likely due to solar-geomagnetic effects (e.g. Sunkara and Tiwari, 2016). Fig. 11 also highlights that, despite a weak positive trend in the ITD latitude, there has been a slight southward displacement since 2010. A possible explanation is the shift to more negative IOD events, co-occurring with the more frequent La Nina episodes (e.g. Niranjan Kumar and Ouarda, 2004; Lestari and Koh, 2016).

5. Conclusions

In this paper, the climatologically mean state and variability of the AHL and ITD are investigated over the Arabian Peninsula with the 1979-2019 ERA-5 reanalysis data. The usage of ERA-5 data, which has high spatial (0.25º or ~27 km) and temporal (hourly) resolution compared to other reanalysis datasets, is justified, as a comparison with hourly data at individual stations in the region revealed a good agreement with the observed air temperature and sea-level pressure. The AHL is a deep thermal low that develops in response to the strong surface heating, and is therefore mostly a summertime feature. The ITD denotes the boundary between the hot and dry air from the Arabian Desert and the cooler and moist marine air from the Arabian Sea. Both features have been extensively investigated over Africa, but not so much over southwestern Asia, where only the ITD was discussed and for individual case studies.

The AHL is typically detected with a LLAT, $\theta_{850\ hPa}$, sea-level pressure or $\xi_{850\ hPa}$ diagnostic. Here, the LLAT-based methodology proposed by Lavaysse *et al.* (2009) is employed over the region 10º-35ºN and 40º-60ºE at 03 UTC (before local sunrise). The AHL is found to exhibit variability on intra-seasonal time-scales, in association with the active and break periods of the Indian Summer Monsoon (e.g. Attada *et al.*, 2019): increased convective activity and ascent over the Arabian Sea and Indian subcontinent lead to descent and adiabatic warming over the Arabian Peninsula, and hence to a stronger AHL. This feature also shows a pronounced diurnal variability, with a maximum at 14 UTC (18 LT) and a minimum at 05 UTC (09 LT). The phase is largely invariant from June to September, with the highest amplitudes seen in July. Over the 41-year period, the AHL shows a strengthening that is statistically significant at the 95% confidence interval, in line with the observed surface warming in the region (Almazroui *et al.*, 2014). However, no clear shift in its position is noted. On inter-annual timescales, ENSO and IOD play an important role in the AHL's variability, as they modulate the convective activity in the Indian Ocean.

The ITD is identified using moisture-based and/or wind-based diagnostics. Here, a 15ºC threshold in the dew-point temperature is used to detect the ITD at 00 UTC. In the cold season, the ITD is located along the Arabian Peninsula coastline, but it migrates northward starting in April, and reaches up to 28ºN just to the west of 60ºE in particular in July and August. In the western Arabian Peninsula, it shows a rather small diurnal variability, being located mostly along the southern Saudi Arabian coastline, while in the eastern side, and in the warm season, its position can fluctuate by as much as 10º, reaching the Arabian Gulf and southern Iranian coastline at night. A comparison between a real-case and a semi-idealised numerical simulation where the orography is removed for a 7-day period in July 2018, revealed that the coastal position of the ITD is due to the presence of topography, as without it the ITD is placed well inland over the full southern Saudi Arabia. Only a weak positive trend, but statistically significant at the 95% confidence level, in the location of the ITD is seen in the data, likely driven by the increased SSTs in the Arabian Sea and Arabian Gulf. While ENSO and IOD seem to account for a significant fraction of the inter-annual variability of the ITD, like the AHL, the signal from solar-geomagnetic effects (e.g. Misios *et al.*, 2016; Sunkara and Tiwari, 2016) is also clearly seen in a wavelet analysis. Positive IOD events promote a northward migration of the ITD, as La Nina events also do.

It is important to note that the AHL and ITD are interrelated, as the strengthening of the AHL will lead to the advance of the opposing flows towards it and a northward displacement of the ITD. Both features play a crucial role in the weather conditions in the Arabian Peninsula by modulating the atmospheric circulation at different altitudes. For instance, the ITD helps in triggering dust storms and convective events (e.g., Francis et al., 2020b; 2021) as convergence zones promote ascent and favour cloud development while increasing near-surface turbulence which favors dust uplift. An extension of this work would include investigating how processes such as dust storms, convection initiation, and sea- and land-breeze circulations are modulated by the AHL and ITD.

Acknowledgments

We would like to acknowledge the Copernicus Programme for making the ERA-5 reanalysis data freely available through the Climate Change Service portal (https://climate.copernicus.eu/climate-reanalysis). We wish to acknowledge the contribution of Khalifa University's high-performance computing and research computing facilities to the results of this research. We would also like to thank two anonymous reviewers for their several detailed and insightful comments that helped to significantly improve the quality of the paper.

Conflict of Interest: The authors declare they have no conflict of interest.

References

Ackerman, S. A. and Cox, S. K. (1982) The Saudi Arabian heat low: Aerosol distributions and thermodynamic structure. Journal of Geophysical Research, 87, 8991-9002.

Alapaty, K., Herwehe, J., Otte, T. L., Nolte, C. G., Bullock, O. R., Mallard, M. S., Kain, J. S. and Dudhia, J. (2012) Introducing subgrid-scale cloud feedbacks to radiation for regional meteorological and climate modeling. Geophysical Research Letters, 39, 24809. https://doi.org/10.1029/2012GL054031.

Aldababseh, A. and Temimi, M. (2017) Analysis of the Long-Term Variability of Poor Visibility Events in the UAE and the Link with Climate Dynamics. Atmosphere, 8, 242. https://doi.org/10.3390/atmos8120242

Almazroui, M., Islam, M. N., Dambul, R. and Jones, P. D. (2014) Trends of temperature extremes in Saudi Arabia. International Journal of Climatology, 34, 808-826

Al Senafi, F. and Anis, A. (2015) Shamals and climate variability in the Northern Arabian/Persian Gulf from 1973 to 2012. International Journal of Climatology, 35, 4509-4528.

Anil, N., Kumar, M. R. R., Sajeev, R. and Saji, P. K. (2016) Role of distinct flavours of IOD events on Indian summer monsoon. Natural Hazards, 82, 1317-1326.

Attada, R., Dasari, H. P., Parekh, A., Chowdary, J. S., Langodan, S., Knio, O. and Hoteit, I. (2019) The role of the Indian Summer Monsoon variability on Arabian Peninsula summer climate. Climate Dynamics, 52, 3389-3404.

Babu, C. A., Jayakrishnan, P. R. and Varikoden, H. (2016) Characteristics of precipitation pattern in the Arabian Peninsula and its variability associated with ENSO. Arabian Journal of Geosciences, 9, 186. https://doi.org/10.1007/s12517-015-2265-x.

Berner, J., Christensen, H. M. and Sardeshmukh, P. D. (2020) Does ENSO Regularity Increase in a Warming Climate? Journal of Climate, 33, 1247-1259.

Blake, D. W., Krishnamurti, T. N., Low-Nam, S. V. and Fein, J. S. (1983) Heat low over the Saudi Arabian desert during May 1979 (Summer MONEX). Monthly Weather Review, 9, 1759-1775.

Bou Karam, D., Flamant, C., Knippertz, P., Reitebuch, O., Pelon, J., Chong, M. and Dabas, A. (2008) Dust emissions over the Sahel associated with the West African monsoon intertropical discontinuity region: A representative case-study. Quarterly Journal of the Royal Meteorological Society, 134, 621-634.

Bou Karam, D., Flamant, C., Tulet, P., Chaboureau, J.-P., Dabas, A. and Todd, M. C. (2009a) Estimate of Sahelian dust emissions in the inter-tropical discontinuity region of the West African Monsoon. Journal of Geophysical Research, 114, D13106. https://doi.org/10.1029/2008JD011444.

Bou Karam, D., Flamant, C., Tulet, P., Todd, M. C., Pelon, J. and Williams, E. (2009b) Dry cyclogenesis and dust mobilization in the intertropical discontinuity of the West Africa Monsoon: A case study. Journal of Geophysical Research, 114, D015115. https://doi.org/10.1029/2008JD010952.

Bou Karam, D., E. Williams, M. Janiga, C. Flamant, M. MacGraw-Herdeg, J. Cuesta, A. Auby, C. Thorncroft (2014), Synoptic-scale dust emissions over the Sahara Desert initiated by a moist convective cold pool in early August 2006, Quarterly Journal of the Royal Meteorological Society, DOI: 10.1002/qj2326.

Branch, O., Behrendt, A., Gong, Z., Schwitalla, T. and Wulfmeyer, V. (2020) Convection Initiation over the East Arabian Peninsula. Meteorologische Zeitschrift, 29, 67-77.

Buckle, C. (1996) Weather and Climate in Africa. Addison-Wesley Longman Ltd. Harlow, U.K.

Chaboureau, J.-P., Flamant, C., Dauhut, T., Kocha, C., Lafore, J.-P., Lavaysse, C., Marnas, F., Mokhtari, M., Pelon, J., Martinez, I. R., Schepanski, K. and Tulet, P. (2016) Fennec dust forecast intercomparison over the Sahara in June 2011. Atmospheric Chemistry and Physics, 16, 6977-6995.

Chaouch, N., Temimi, M., Weston, M. and Ghedira, H. (2017) Sensitivity of the meteorological model WRF-ARW to planetary boundary layer schemes during fog conditions in a coastal arid region. Atmospheric Research, 187, 106-127.

Chauvin, F., Roehrig, R. and Lafore, J. (2010) Intraseasonal Variability of the Saharan Heat Low and its Link with Midlatitudes. Journal of Climate, 23, 2544-2561.

Cosnefroy, H., Leroy, M and Briottet, X. (1996) Selection and characterization of Saharan and Arabian desert sites for the calibration of optical satellite sensors. Remote Sensing of the Environment, 58, 101-114.

Dumka, U. C., Kaskaoutis, D. G., Francis, D., Chaboureau, J.-P., Rashki, A., Tiwari, S., Singh, S., Liakokou, E. and Mihalopoulos, N. (2019) The role of the Intertropical Discontinuity region and the heat low in dust emission and transport over the Thar desert, India: A premonsoon case study. Journal of Geophysical Research: Atmospheres, 124, 13197-13219.

Eager, R. E., Raman, S., Wootten, A., Westphal, D. L., Reid, J. S. and Al Mandoos, A. (2008) A climatological study of the sea and land breezes in the Arabian Gulf region. Journal of Geophysical Research, 113, D15106. https://doi.org/10.1029/2007JD009710.

Engelstaedter, S., Washington, R., Flamant, C., Parker, D. J., Allen, C. J. T. and Todd, M. C. (2015) The Saharan heat low and moisture transport pathways in the central Sahara - Multiaircraft observations and Africa-LAM evaluation. Journal of Geophysical Research: Atmospheres, 120, 4417-4442.

Fekih, A. and Mohamed, A. (2019) Evaluation of the WRF model on simulating the vertical structure and diurnal cycle of the atmospheric boundary layer over Bordj Badji Mokhtar (southwestern Algeria). Journal of King Saud University - Science, 31, 602-611.

Flamant, C., Chaboureau, J.-P., Parker, D. J., Taylor, C. M., Cammas, J.-P., Bock, O., Timouk, F. and Pelon, J. (2007) Airborne observations of the impact of a convective system on the planetary boundary layer thermodynamics and aerosol distribution in the inter-tropical discontinuity region of the West African Monsoon. Quarterly Journal of the Royal Meteorological Society, 133, 1175-1189.

Flamant, C., Knippertz, P., Parker, D. J., Chaboureau, J.-P., Lavaysse, C., Agusti-Panareda, A. and Kergoat, L. (2009) The impact of a mesoscale convective system cold pool on the northward propagation of the intertropical discontinuity over West Africa. Quarterly Journal of the Royal Meteorological Society, 135, 139-159.

Fletcher, R. D. (1945) The General Circulation of the Tropical and Equatorial Atmosphere. Journal of Meteorology, 2, 167-174.

Francis, D., Fonseca, R., Nelli, N., Cuesta, J., Weston, M., Evan, A. and Temimi, M. (2020a). The atmospheric drivers of the major Saharan dust storm in June 2020. Geophysical Research Letters, 47, e2020GL090102. https://doi.org/10.1029/2020GL090102

Francis D., J-P. Chaboureau, N. Nelli, et al., (2020b), Summertime dust storms over the Arabian Peninsula and impacts on radiation, circulation, cloud development and rain, Atmospheric Research, 2020, 105364, ISSN 0169-8095. https://doi.org/10.1016/j.atmosres.2020.105364.

Francis, D., Temimi, M., Fonseca, R., Nelli, N. R., Abida, R., Weston, M. and Wehbe, Y. (2021) On the Analysis of a Summertime Convective Event in a Hyperarid Environment. Quarterly Journal of the Royal Meteorological Society, 147, 501-525.

Grams, C. M., Jones, S. C., Marsham, J. H., Parker, D. J., Haywood, J. M. and Heuveline, V. (2010) The Atlantic inflow to the Saharan heat low: Observations and Modelling. Quarterly Journal of the Royal Meteorological Society, 136, 125-140.

Hamilton, R. A. and J. W. Archibald (1945) Meteorology of Nigeria and adjacent territory, Quarterly Journal of the Royal Meteorological Society, 71, 231– 265.

Hersbach, H., Bell, B., Berrisford, P., Hirahara, S., Horanyi, A., Munoz-Sabater, J., Nicolas, J., Peubey, C., Radu, R., Schepers, D., Simmons, A., Soci, C., Abdalla, S., Abellan, X., Balsamo, G., Bachtold, P., Biavati, G., Bidlot, J., Bonavita, M., De Chiara, G., Dahlgren, P., Dee, D., Diamantakis, M., Dragani, R., Flemming, J., Forbes, R., Fuentes, M., Geer, A., Haimberger, L., Healy, S., Hogan, R. J., Holm, E., Janiskova, M., Keeley, S., Laloyaux, P., Lopez, P., Lupu, C., Radnoti, G., de Rosnay, P., Rozum, I., Vamborg, F., Villaume, S. and Thepaut, J.-N. (2020) The ERA5 global reanalysis. Quarterly Journal of the Royal Meteorological Society, 146, 1999-2049.

Hrudya, P. H., Varikoden, H. and Vishnu, R. (2020) A review on the Indian summer monsoon rainfall, variability and its association with ENSO and IOD. Meteorology and Atmospheric Physics. https://doi.org/10.1007/s00703-020-00734-5.

Huang, B., Thorne, P. W., Banzon, V. F., Boyer, T., Chepurin, G., Lawrimore, J. H., Menne, M. J., Smith, T. M., Vose, R. S. and Zhang, H.-M. (2017) Extended Reconstructed Sea Surface Temperature, Version 5 (ERSSTv5): Upgrades, Validations, and Intercomparisons. Journal of Climate, 30, 8179-8205.

Iacono, M. J., Delamere, J. S., Mlawer, E. J., Shephard, M. W., Clough, S. A., and Collins, W. D. (2008) Radiative forcing by long-lived greenhouse gases: calculations with the AER radiative transfer models. Journal of Geophysical Research, 113, D13103. https://doi.org/10.1029/2008JD009944.

Kain, J. S. (2004) The Kain-Fritsch convective parameterization: an update. Journal of Applied Meteorology, 43, 170-181.

Kalapureddy, M. C. R., Lothon, M., Campistron, B., Lohoub, F. and Said, F. (2010) Wind profiler analysis of the African Easterly Jet in relation with the boundary layer and the Saharan heat-low. Quarterly Journal of the Royal Meteorological Society, 136, 77-91.

Karagulian, F., Temimi, M., Ghebreyesus, D., Weston, M., Kondapalli, N. K., Valappil, V. K., Aldababseh, A., Lyapustin, A., Chaouch, N., Al Hammadi, F. and Al Abdooli, A. (2019) Analysis of a severe dust storm and its impact on air quality conditions using WRF-Chem modeling, satellite imagery, and ground observations. Air Quality, Atmosphere & Health, 12, 453-470.

Konda, G., Chowdary, J. S., Srinivas, G., Gnanaseelan, C., Parekh, A., Attada, R. and Rama Krishna (2018) Tropospheric biennial oscillation and south Asian summer monsoon rainfall in a coupled model. Journal of Earth System Sciences, 127, 46. https://doi.org/10.1007/s12040-018-0948-x

Knippertz, P. (2008) Dust emissions in the West African heat trough - the role of the diurnal cycle and of extratropical disturbances. Meteorologische Zeitschrift, 17, 553-563.

Kumar, S. P., Roshim. R. P., Narvekar, J., Kuamr, D. and Vivekanandan, E. (2009) Response of the Arabian Sea to global warming and associated regional climate shift. Marine Environmental Research, 68, 217-222.

Lafore, J.-P., Chapelon, N., Beucher, F., Diop-Kane, M., Gaymard, A., Kasimou, A., Lepape, S., Mumbai, Z., Orji, B., Osika, D., Parker, D. J., Poan, E., Razafindrakoto, L. G., Vincendon, J. C., ACMAD and the West Africa forecasting community (2017) West African Synthetic Analysis and Forecast. In Meteorology of Tropical West Africa (eds. D. J. Parker and M. Diop-Kane). https://doi.org/10.1002/9781118391297.ch11

Lavaysse, C., Flamant, C., Janicot, S., Parker, D. J., Lafore, J.-P., Sultan, B. and Pelon, J. (2009) Seasonal evolution of the West African heat low: a climatological perspective. Climate Dynamics, 33, 313-330. https://doi.org/10.1007/s00382-009-0553-4.

Lavaysse, C., Flamant, C. and Janicot, S. (2010) Regional-scale convection patterns during strong and weak phases of the Saharan heat low. Atmospheric Science Letters, 11, 255-264. https://doi.org/10.1002/asl.284

Lavaysse, C., Eymard, L., Flamant, C., Karbou, F., Mimouni, M. and Saci, A. (2013) Monitoring the West African heat low at seasonal and intra-seasonal timescales using AMSU-A sounder. Atmospheric Science Letters, 14, 263-271. https://doi.org/10.1002/asl2.449

Lestari, R. K. and Koh, T.-Y. (2016) Statistical Evidence for Asymmetry in ENSO-IOD Interactions. Atmosphere-Ocean, 54, 498-504.

Lélé, M. I. and P. J. Lamb (2007) Variability of Intertropical Front and rainfall over West African Soudano-Sahel zone. Paper presented at 2^{nd} International African Monsoon Multidisciplinary Analyses Conference, Karlsruhe, Germany, 26 – 30 Nov.

Lyngsie, G., Olsen, J. L., Awadzi, T. W., Fensholdt, R. and Breuning-Madsen, H. (2013) Influence of the inter tropical discontinuity on Harmattan dust deposition in Ghana. Geochemistry, Geophysics, Geosystems, 14, 3425-3435.

Lothon, M., Said, F., Lohou, F. and Campistron, B. (2008) Observation of the Diurnal Cycle in the Low Troposphere of West Africa. Monthly Weather Review, 136, 3477-3500.

Misios, S., Mitchell, D. M., Gray, L. J., Tourpali, K., Matthes, K., Hood, L., Schmidt, H., Chiodo, G., Thieblemont, R., Rozanov, E. and Krivolutsky, A. (2016) Solar signals in CMIP-5 simulations: effects of atmosphere-ocean coupling. Quarterly Journal of the Royal Meteorological Society, 142, 928-941.

Nakanishi, M., and Niino, H. (2006) An Improved Mellor-Yamada Level-3 Model: Its Numerical Stability and Application to a Regional Prediction of Advection Fog. Boundary-Layer Meteorology, 119, 397-407.

Nakanishi, M., and Niino, H. (2009) Development of an Improved Turbulence Closure Model for the Atmospheric Boundary Layer. Journal of the Meteorological Society of Japan, 87, 895-912.

Nelli, N. R., Temimi, M., Fonseca, R. M., Weston, M. J., Thota, M. S., Valappil, V. K., Branch, O., Wizemann, H.-D., Wulfmeyer, V. and Wehbe, Y. (2020a) Micrometeorological measurements in an arid environment: Diurnal characteristics and surface energy balance closure. Atmospheric Research, 104745. https://doi.org/10.1016/j.atmosres.2019.104745

Nelli, N. R., Temimi, M., Fonseca, R. M., Weston, M. J., Thota, M. S., Valappil, V. K., Branch, O., Wulfemeyer, V., Wehbe, Y., Al Hosary, T., Shalaby, A., Al Shamshi, N. and Al Naqbi, H. (2020b) Impact of roughness length on WRF simulated land-atmosphere interactions over a hyperarid region. Earth and Space Science, **7**, e2020EA001165. https://doi.org/10.1029/2020EA001165.

Niranjan Kumar, K. and Ouarda, T. B. M. J. (2014) Precipitation variability over UAE and global SST teleconnections. Journal of Geophysical Research: Atmospheres, 119, 10313-10322.

Niu, G.-Y., Yang, Z. L., Mitchell, K. E., Chen, F., Ek, M. B., Barlage, M., Kumar, A., Manning, K., Niyogi, D., Rosero, E., Tewari, M., and Xia, Y. (2011) The community Noah land surface model with multiparameterization options (Noah-MP): 1. Model description and evaluation with local-scale measurements. Journal of Geophysical Research, 116, D12109. https://doi.org/10.1029/2010JD015139.

Noori, R., Tian, F., Berndtsson, R., Abbasi, M. R., Naseh, M. V., Modabberi, A., Soltani, A. and Klove, B. (2019) Recent and future trends in sea surface temperature across the Persian Gulf and Gulf of Oman. PLoS ONE, 14, e0212790. https://doi.org/10.1371/journal.pone.0212790.

Odekunle, T. O. (2010) An Assessment of the Influence of the Inter-Tropical Discontinuity on Inter-Annual Rainfall Characteristics in Nigeria. Geophysical Research, 48, 314-326.

Odekunle, T. O. and Adejuwon, S. A. (2017) Assessing changes in the rainfall regime in Nigeria between 1961 and 2004. GeoJournal, 70, 145-159.

Parker, D. J. and Diop-Kane, M. (2017) Meteorology of tropical West Africa: The forecasters' handbook. John Wiley & Sons, 468 pp.

Pospichal, B., Bou Karam, D., Crewell, S., Flamant, C., Hunerbein, A., Bock, O. and Said, F. (2010) Diurnal cycle of the intertropical discontinuity over West Africa analysed by remote sensing and mesoscale modelling. Quarterly Journal of the Royal Meteorological Society, 136, 92-106.

Racz, Z. and Smith, R. K. (19990) The dynamics of heat lows. Quarterly Journal of the Royal Meteorological Society, 125, 225-252. https://doi.org/10.1002/qj.49712555313

Rashki, A., Kaskaoutis, D. G., Mofidi, A., Minvielle, F., Chiapello, I., Legrand, M., Dumka, U. C. and Francois, P. (2019) Effects of Monsoon, Shamal and Levar winds on dust accumulation over the Arabian Sea during summer - The July 2016 case. Aeolian Research, 36, 27-44.

Redelsperger, J.-L., Diongue, A., Diehiou, A., Ceron, J.-P., Diop, M., Gueremy, J.-F. and Lafore, J.-P. (2002) Multi-scale description of a Sahelian synoptic weather system representative of the West African monsoon. Quarterly Journal of the Royal Meteorological Society, 128, 1229-1257.

Roehrig, R., Chauvin, F. and Lafore, J. (2011) 10-25 Day Intraseasonal Variability of Convection over the Sahel: A Role of the Saharan Heat Low and Midlatitudes. Journal of Climate, 24, 5863-5878.

Saji, N. H., Goswami, B. N., Vinayachandran, P. N. and Yamagata, T. (1999) A dipole mode in the tropical Indian Ocean. Nature, 401, 360-363.

Schott, F. A., Xie, S.-P. and McCreary Jr., J. P. (2009) Indian Ocean circulation and climate variability. Reviews of Geophysics, 47, RG1002. https://doi.org/10.1029/2007RG000245.

Schwitalla, T., Branch, O. and Wulfmeyer, V. (2020) Sensitivity study of the planetary boundary layer microphysical schemes to the initialization of convection over the Arabian Peninsula. Quarterly Journal of the Royal Meteorological Society, 146, 846-869.

Skamarock, W. C., Klemp, J. B., Dudhia, J., Gill, D. O., Barker, D. M., Duda, M. G., Huang, X.-Y., Wang, W., and Powers, J. G. (2008) A description of the Advanced Research WRF version 3, 113 pp. https://dx.doi.org/10.5065/D68S4MVH.

Smith, E. A. (1986a) The Structure of the Arabian Heat Low. Part I: Surface Energy Budget. Monthly Weather Review, 114, 1067-1083.

Smith, E. A. (1986b) The Structure of the Arabian Heat Low. Part II: Bulk Tropospheric Heat Budget and Implications. Monthly Weather Review, 114, 1084-1102.

Spengler, T., and Smith, R. K. (2008) The dynamics of heat lows over flat terrain. Quarterly Journal of the Royal Meteorological Society, 134, 2157-2172.

Spinks, J., Lin, Y.-L., and Mekonnen, A. (2015) Effects of the subtropical anticylonic over North Africa and Arabian Peninsula on the Africa easterly jet. International Journal of Climatology, 35, 733-745.

Srivastava, G., Chakraborty, A. and Nanjundiah, R. S. (2020) Multidecadal variations in ENSO-Indian summer monsoon relationship at sub-seasonal timescales. Theoretical and Applied Climatology, 140, 1299-1314.

Steinhoff, D. F., Bruintjes, R., Hacker, J., Keller, T., Williams, C., Jensen, T., Al Mandous, A. and Al Yazeedi, O. A. (2018) Influences of the Monsoon Trough and Arabian Heat Low on Summer Rainfall over the United Arab Emirates. Monthly Weather Review, 146, 1383-1403.

Sultan, B. and Janicot, S. (2003) The West African Monsoon Dynamics. Part II: The "Preonset" and "Onset" of the Summer Monsoon. Journal of Climate, 16, 3407-3427.

Sultan, B., Janicot, S. and Drobinski, P. (2007) Characterization of the diurnal cycle of the West African monsoon around the monsoon onset. Journal of Climate, 20, 4014-4032.

Sunkara, S. L. and Tiwari, R. K. (2016) Wavelet analysis of the singular spectral reconstructed time series to study the impacts of solar-ENSO-geomagnetic activity on Indian Climate. Nonlinear Processes in Geophysics, 23, 361-374.

Temimi, M., Fonseca, R., Nelli, N., Weston, M., Thota, M., Valappil, V., Branch, O., Wizemann, H.-D., Kondapalli, N. K., Wehbe, Y., Al Hosary, T., Shalaby, A., Al Shamsi, N. and Al Naqbi, H.

(2020) Assessing The Impact of Changes in Land Surface Conditions on WRF Predictions in Arid Regions. Journal of Hydrometeorology, 1-60. https://doi.org/10.1175/JHM-D-20-0083.1.

Thompson, G., and Eidhammer, T. (2014) A Study of Aerosol Impacts on Clouds and Precipitation Development in a Large Winter Cyclone. Journal of the Atmospheric Sciences, 71, 3636-3658.

Waliser, D. E. and Gautier, C. (1993) A Satellite-derived Climatology of the ITCZ. Journal of Climate, 6, 2162-2174.

Wang, W., Evan, A. T., Flamant, C. and Lavaysse, C. (2015) On the decadal scale correlation between African dust and Sahel rainfall: The role of Saharan heat low-forced winds. Science Advances, 9, e1500646. https://doi.org/10.1126/sciadv.1500646.

Wang, W., Evan, A. T., Lavaysse, C. and Flamant, C. (2017) The role the Saharan Heat Low plays in dust emission and transport during summertime in North Africa. Aeolian Research, 28, 1-12.

Wang, H., Kumar, A., Murtugudde, R., Narapusetty, B. and Seip, K. L. (2019) Covariations between the Indian Ocean dipole and ENSO: a modeling study. Climate Dynamics, 53, 5743-5761.

Wehbe, Y., Temimi, M. and Adler, R. F. (2020) Enhancing Precipitation Estimates Through the Fusion of Weather Radar, Satellite Retrievals, and Surface Parameters. Remote Sensing, 12, 1342. https://doi.org/10.3390/rs12081342

Wehbe, Y., Temimi, M., Ghebreyesus, D. T., Milewski, A., Norouzi, H. and Ibrahim, E. (2018) Consistency of precipitation products over the Arabian Peninsula and interactions with soil moisture and water storage. Hydrological Sciences Journal, 63, 408-425.

Wehbe, Y., Temimi, M., Weston, M., Chaouch, N., Branch, O., Schwitalla, T., Wulfmeyer, V., Zhan, X., Liu, J. and Al Mandous, A. (2019) Analysis of an extreme weather event in a hyper-arid region using WRF-Hydro coupling, station, and satellite data. Natural Hazards and Earth System Sciences, 19, 1129-1149.

Weller, E., Jakob, C. and Reeder, M. J. (2019) Understanding the dynamic contribution to future changes in tropical precipitation from low-level convergence lines. Geophysical Research Letters, 46, 2196-2203.

Weston, M., Chaouch, N., Valappil, V., Temimi, M., Ek, M. and Zheng, W. (2018) Assessment of the sensitivity to the thermal roughness length in Noah and Noah-MP land surface model using WRF in an arid region. Pure and Applied Geophysics, 175, 1-17.

Williams, E. R. (2008) Comment on “Atmospheric controls on the annual cycle of North African dust” by S. Engelstaedter and R. Washington. Journal of Geophysical Research, 113, D23109. https://doi.org/10.1029/2008JD009930.

Xue, P. and Eltahir, E. A. B. (2015) Estimation of the Heat and Water Budgets of the Persian (Arabian) Gulf Using a Regional Climate Model. Journal of Climate, 28, 5041-5062.

Yang, Z.-L., Mitchell, K. E., Chen, F., Ek, M. B., Barlage, M., Kumar, A., Manning, K., Niyogi, D., Rosero, E., Tewari, M., and Xia, Y. (2011) The community Noah land surface model with multiparameterization options (Noah-MP): 2. Evaluation over global river basins. Journal of Geophysical Research, 116, D12110. https://doi.org/10.1029/2010JD015140.

Yu, Y., Notaro, M. Kalashnikova, O. V. and Garay, M. J. (2016) Climatology of summer Shamal wind in the Middle East. Journal of Geophysical Research: Atmospheres, 121, 289-305.

Parameterization Scheme	Option
Cloud Microphysics	Thompson aerosol-aware scheme (Thompson and Eidhammer, 2014)
Planetary Boundary Layer (PBL)	Mellor-Yamada Nakanishi Niino (MYNN) Level 2.5 (Nakanishi and Niino, 2006, 2009)
Radiation	Rapid Radiative Transfer Model for Global Circulation Models (Iacono et al., 2008)
Cumulus	Kain-Fritsch (Kain, 2004), with subgrid-scale cloud feedbacks to radiation (Alapaty et al., 2012)
Land Surface Model (LSM)	Noah LSM with MultiParameterization options, Noah-MP (Niu et al., 2011; Yang et al., 2011)

Table 1: Physics parameterization schemes used in the WRF simulations.

(a)

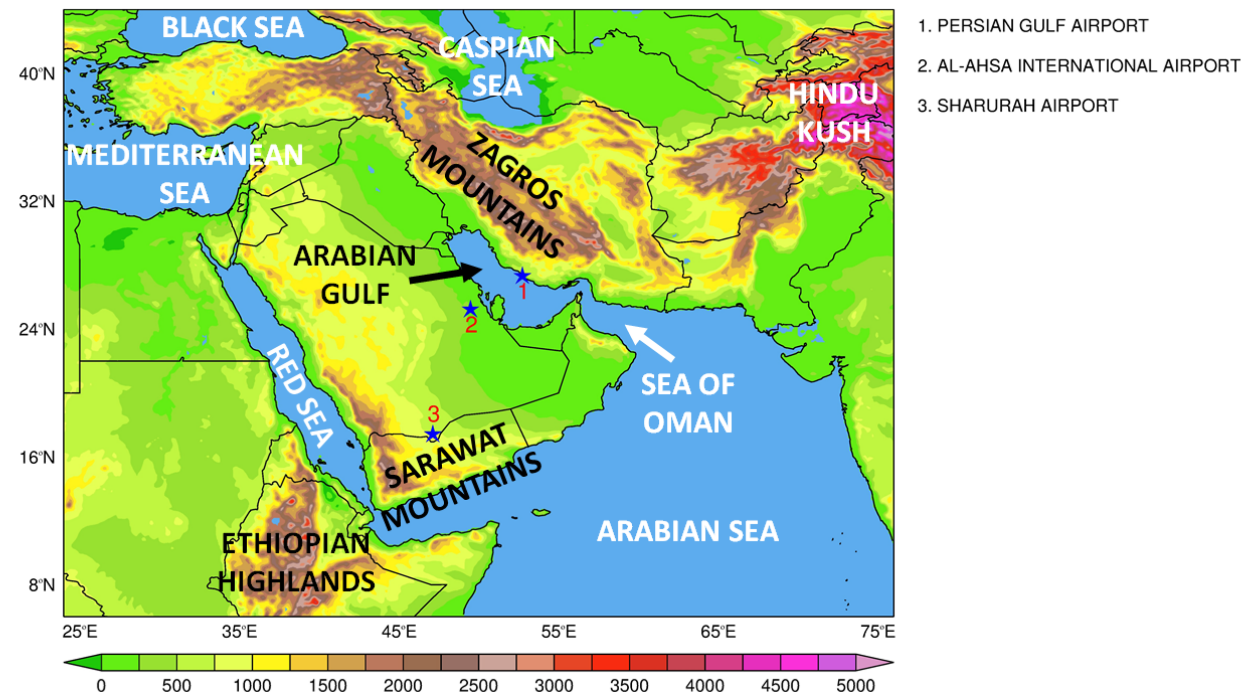
1. PERSIAN GULF AIRPORT
2. AL-AHSA INTERNATIONAL AIRPORT
3. SHARURAH AIRPORT
BLACK SEA
CASPIAN SEA
HINDU KUSH
MEDITERRANEAN SEA
ZAGROS MOUNTAINS
ARABIAN GULF
RED SEA
SEA OF OMAN
SARAWAT MOUNTAINS
ARABIAN SEA
ETHIOPIAN HIGHLANDS
40°N
32°N
24°N
16°N
8°N
25°E
35°E
45°E
55°E
65°E
75°E
0
500
1000
1500
2000
2500
3000
3500
4000
4500
5000

(b)

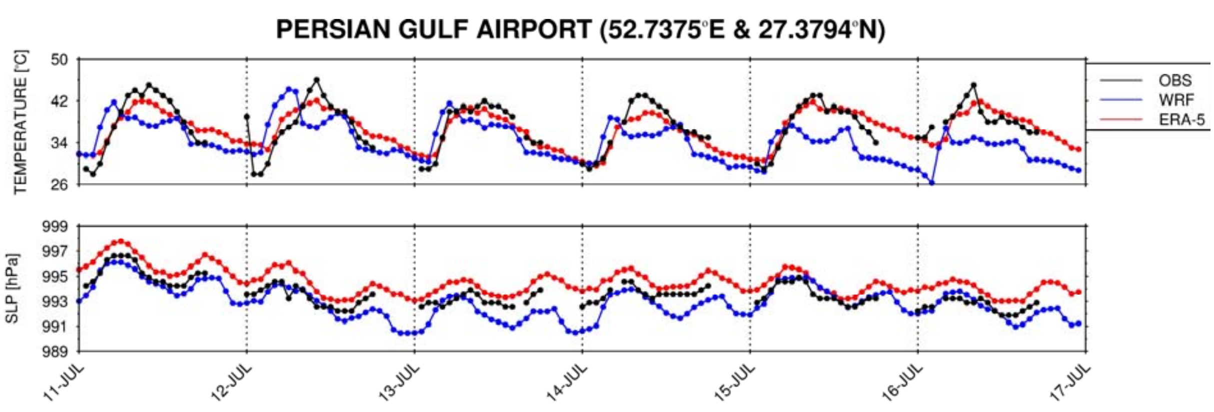
PERSIAN GULF AIRPORT (52.7375°E & 27.3794°N)
TEMPERATURE [°C]
OBS
WRF
ERA-5
SLP [hPa]
11-JUL
12-JUL
13-JUL
14-JUL
15-JUL
16-JUL
17-JUL

(c)

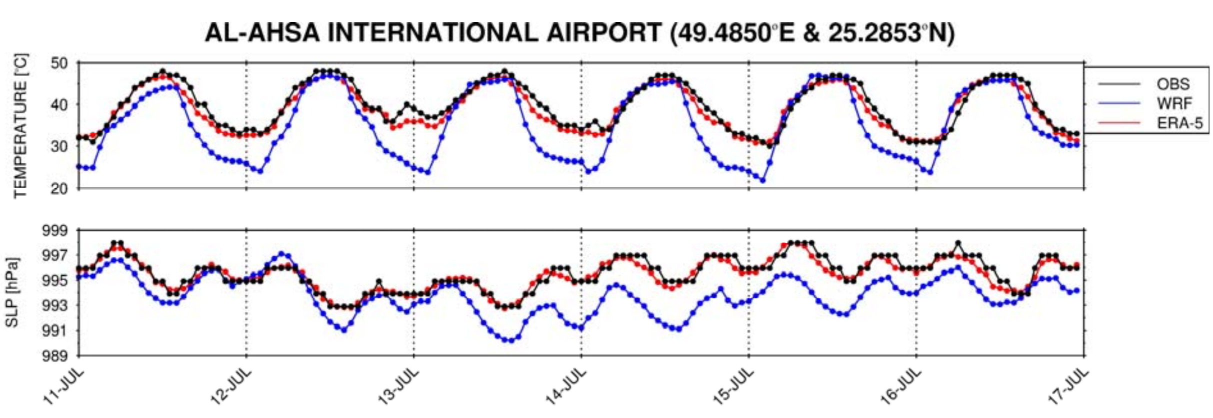
AL-AHSA INTERNATIONAL AIRPORT (49.4850°E & 25.2853°N)
TEMPERATURE [°C]
OBS
WRF
ERA-5
SLP [hPa]
11-JUL
12-JUL
13-JUL
14-JUL
15-JUL
16-JUL
17-JUL

(d)

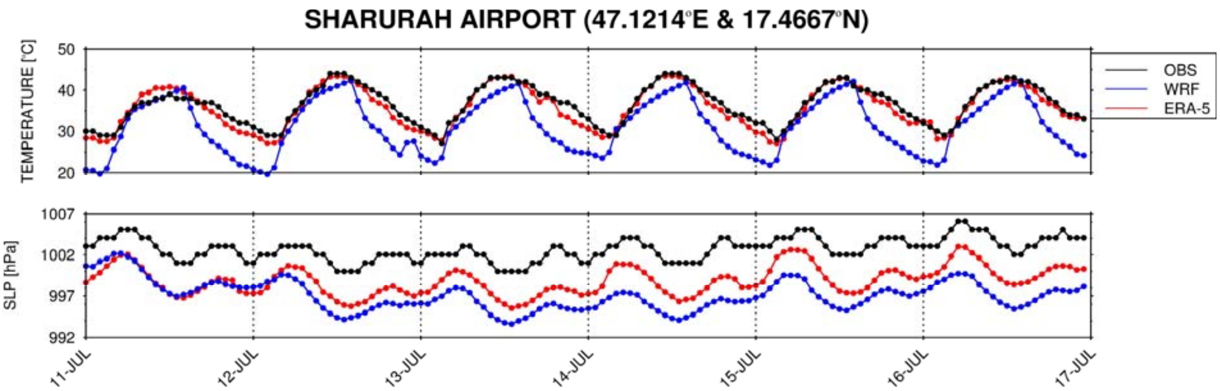

Figure 1: (a) Orography (m) and spatial extent of the WRF model's 12 km domain. (b)-(d) comparison of the observed (black), ERA-5 (red) and WRF-predicted (blue) hourly air temperature (ºC) and sea-level pressure (hPa) at the location of the three stations highlighted by a star in (a). The time is given in UTC.

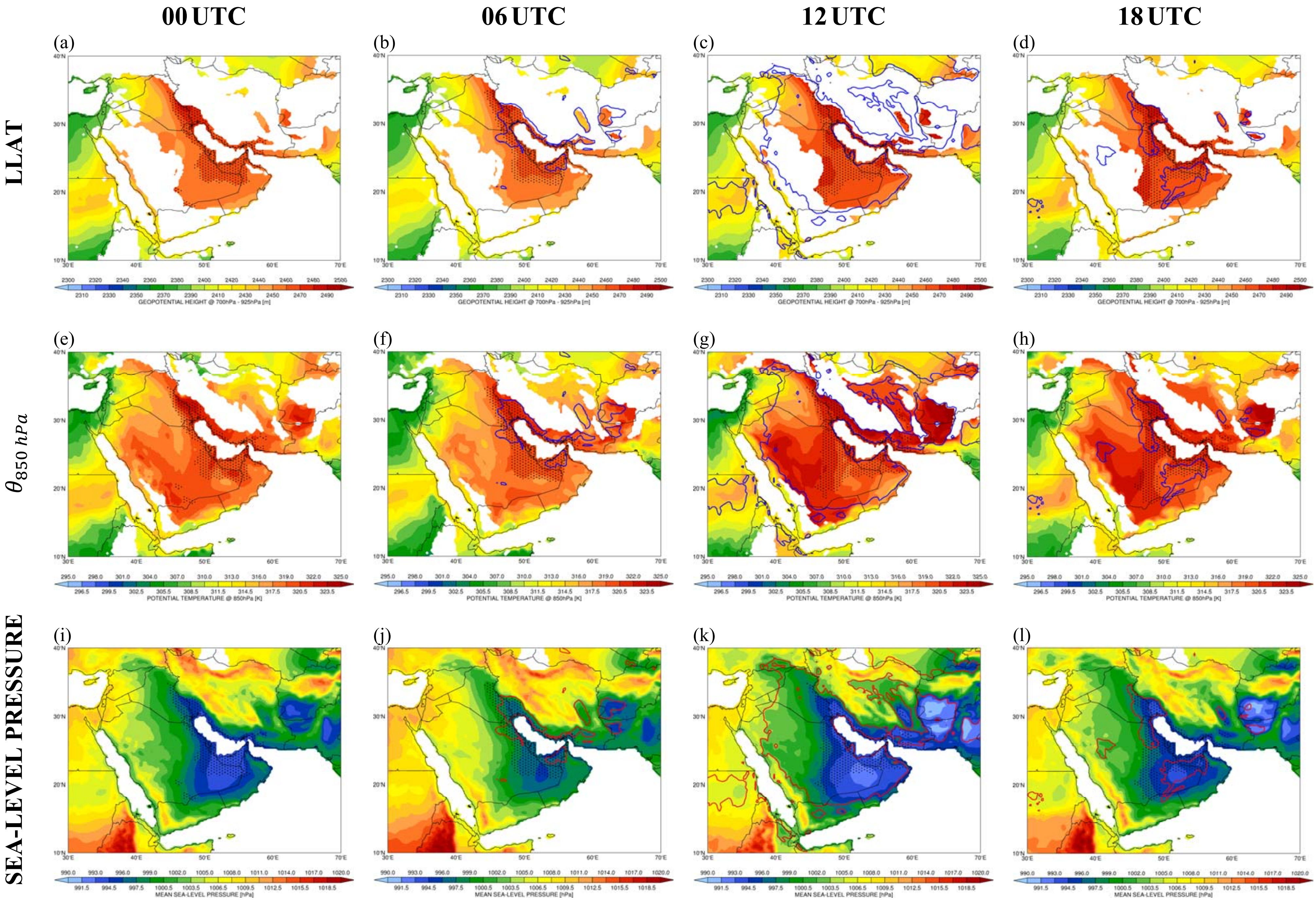
00 UTC
06 UTC
12 UTC
18 UTC
LLAT
$\theta_{850\ hPa}$
SEA-LEVEL PRESSURE
(a)
(b)
(c)
(d)
(e)
(f)
(g)
(h)
(i)
(j)
(k)
(l)
GEOPOTENTIAL HEIGHT @ 700hPa - 925hPa [m]
POTENTIAL TEMPERATURE @ 850hPa [K]
MEAN SEA-LEVEL PRESSURE [hPa]

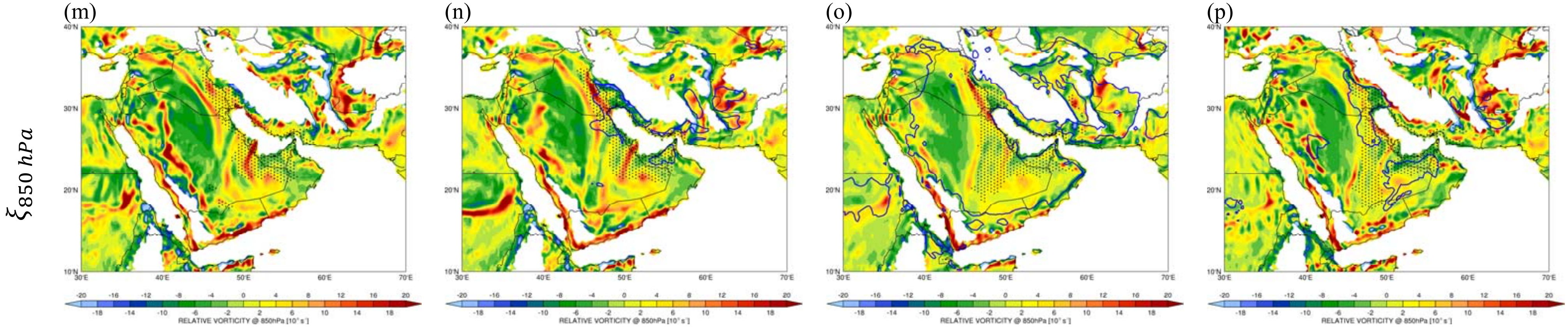

Figure 2: Low-level (700 - 925 hPa) atmospheric thickness (m) at (a) 00, (b) 06, (c) 12 and (d) 18 UTC on 11 July 2018 from ERA-5. The dotted region gives the Arabian Heat Low (AHL), defined as the area with the 10% highest 700 - 925 hPa thickness in the domain 40º-60ºE and 10ºN-35ºN, following Lavaysse *et al.* (2009). The solid contour is the 2-temperature equal to 40ºC isotherm. (e)-(h) is as (a)-(d) but for the 850 hPa potential temperature (K), (i)-(l) is as (a)-(d) but for the mean sea-level pressure (hPa), while in (m)-(p) the 850 hPa relative vorticity (10^{-5} s^{-1}) is plotted. White shading denotes regions where the 925 hPa pressure level is below the surface in panels (a)-(d), and where the 850 hPa pressure level is below the surface in panels (e)-(h) and (m)-(p). Water bodies are also shaded in white.

(a)

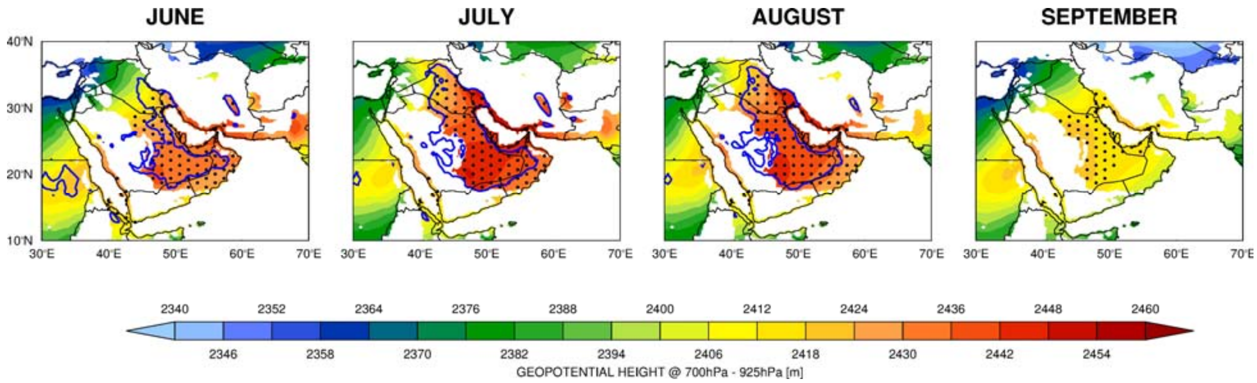
JUNE
JULY
AUGUST
SEPTEMBER
40°N
30°N
20°N
10°N
30°E
40°E
50°E
60°E
70°E
2340 2352 2364 2376 2388 2400 2412 2424 2436 2448 2460
2346 2358 2370 2382 2394 2406 2418 2430 2442 2454
GEOPOTENTIAL HEIGHT @ 700hPa - 925hPa [m]

(b)

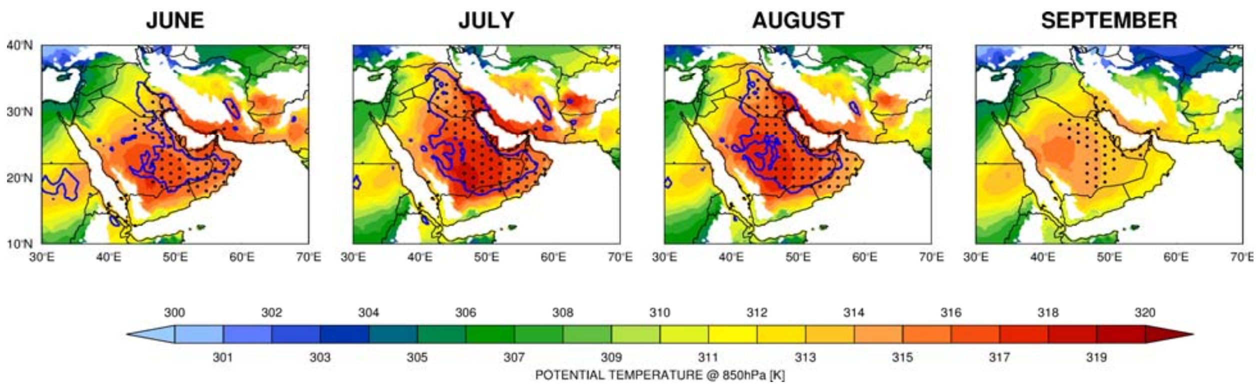
JUNE
JULY
AUGUST
SEPTEMBER
40°N
30°N
20°N
10°N
30°E
40°E
50°E
60°E
70°E
300 302 304 306 308 310 312 314 316 318 320
301 303 305 307 309 311 313 315 317 319
POTENTIAL TEMPERATURE @ 850hPa [K]

(c)

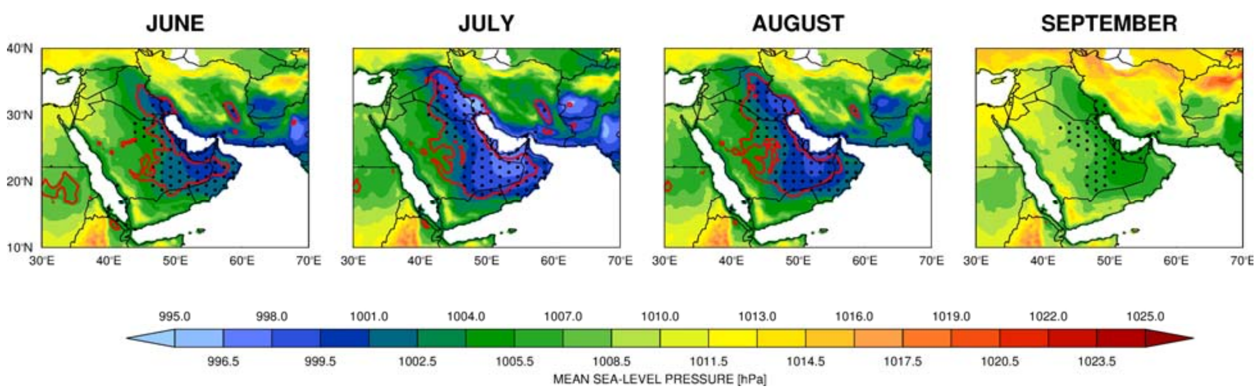
JUNE
JULY
AUGUST
SEPTEMBER
40°N
30°N
20°N
10°N
30°E
40°E
50°E
60°E
70°E
995.0 998.0 1001.0 1004.0 1007.0 1010.0 1013.0 1016.0 1019.0 1022.0 1025.0
996.5 999.5 1002.5 1005.5 1008.5 1011.5 1014.5 1017.5 1020.5 1023.5
MEAN SEA-LEVEL PRESSURE [hPa]

(d)

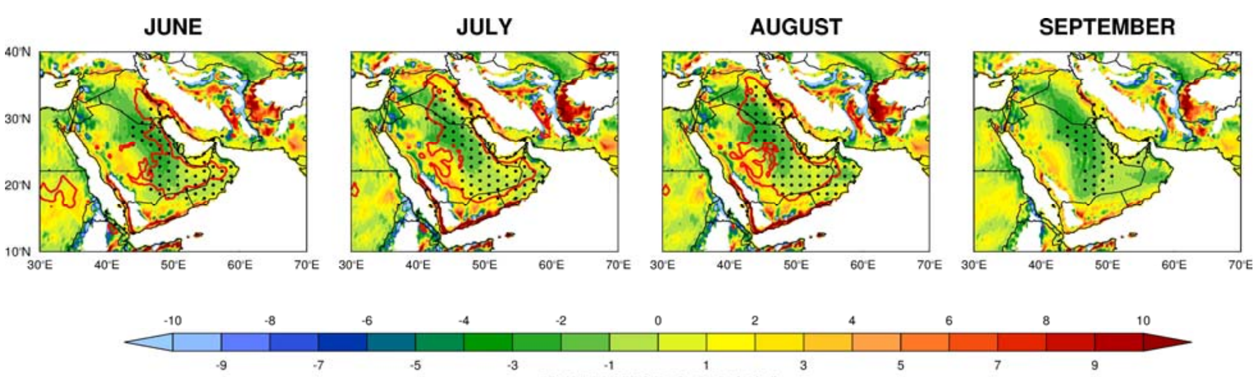
JUNE
JULY
AUGUST
SEPTEMBER
40°N
30°N
20°N
10°N
30°E
40°E
50°E
60°E
70°E
-10 -8 -6 -4 -2 0 2 4 6 8 10
-9 -7 -5 -3 -1 1 3 5 7 9
RELATIVE VORTICITY @ 850hPa [10^{-5} s^{-1}]

Figure 3: June to September monthly mean (a) low-level (700 - 925 hPa) atmospheric thickness (m), (b) 850 hPa potential temperature (K), (c) mean sea-level pressure (hPa), and (d) 850 hPa relative vorticity (10^{-5} s^{-1}) at 03 UTC. The fields are taken from ERA-5 reanalysis data, and are averaged over 1979-2019. The stippled region gives the Arabian Heat Low (AHL), defined as the area with the 10% highest 700 - 925 hPa thickness in the domain 40º-60ºE and 10ºN-35ºN, following Lavaysse *et al.* (2009). The solid contour in all panels is the 2-meter temperature equal to 40ºC isotherm at 15 UTC, also averaged over the 41-year period. The white shading denotes regions for which the 925 hPa pressure surface in panel (a), and the 850 hPa pressure surface in panels (b) and (d) is below orography. Water bodies are also shaded in white.

(a)

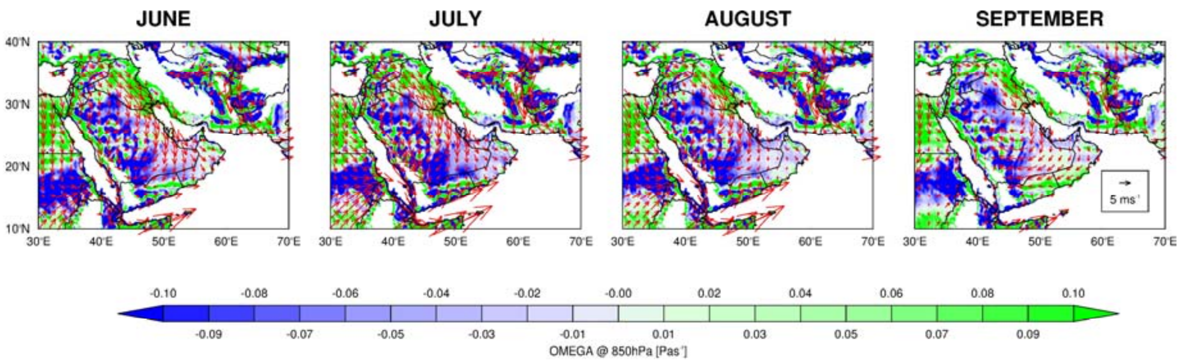

JUNE
JULY
AUGUST
SEPTEMBER
40°N
30°N
20°N
10°N
30°E
40°E
50°E
60°E
70°E
5 ms⁻¹
OMEGA @ 850hPa [Pas⁻¹]

(b)

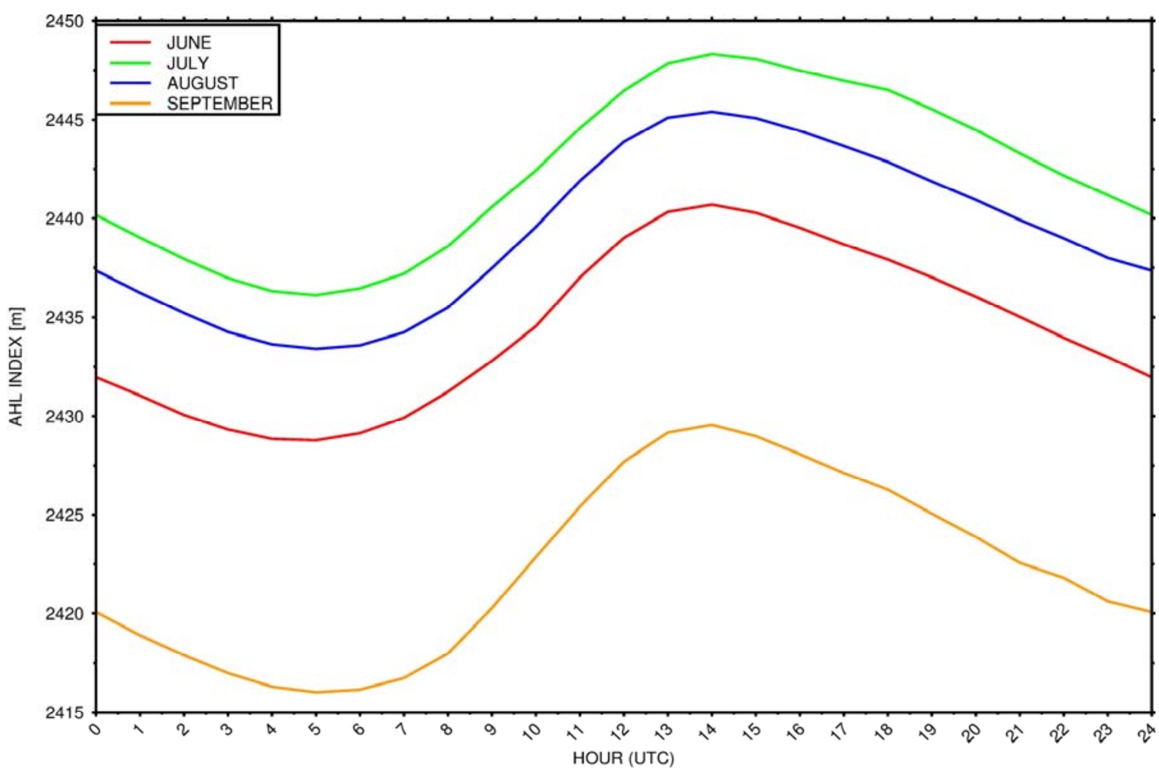

JUNE
JULY
AUGUST
SEPTEMBER
AHL INDEX [m]
HOUR (UTC)

(c)

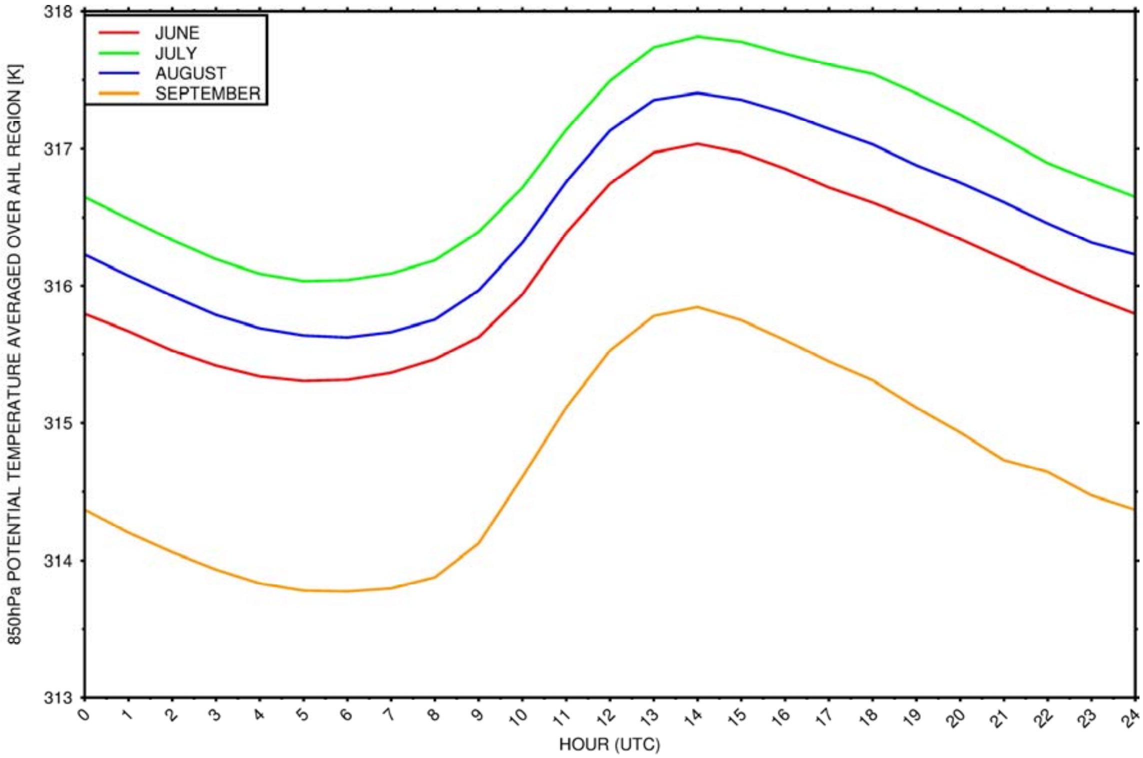

(d)

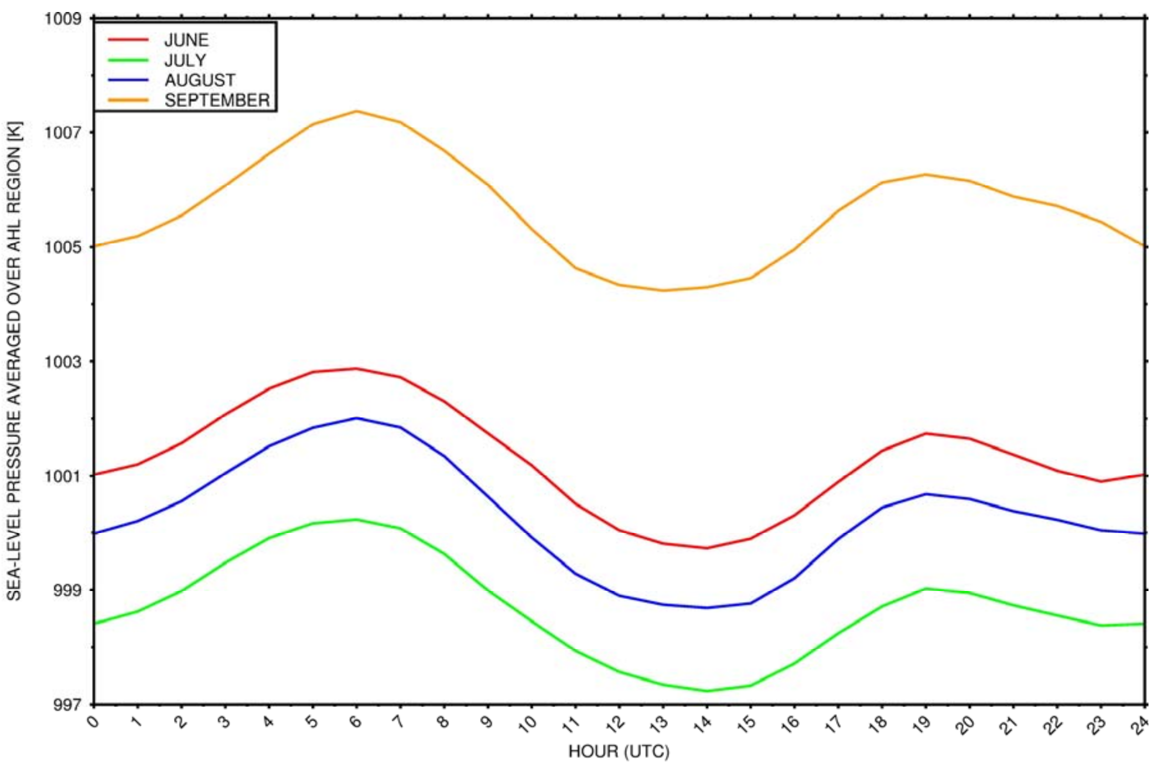

Figure 4: (a) June to September monthly mean 850 hPa omega (shading; Pa s^{-1}) and horizontal wind vectors (arrows; m s^{-1}). (b) Hourly AHL index, defined as the spatial average of the 700 - 925 hPa thickness (m) corresponding to the AHL. The white shading in (a) denotes regions for which the 850 hPa pressure surface is below orography. Both plots are generated with ERA-5 1979-2019 data. (c) and (d) are as (b) but showing the 850 hPa potential temperature (K) and sea-level pressure (hPa) averaged over the AHL region.

(a)

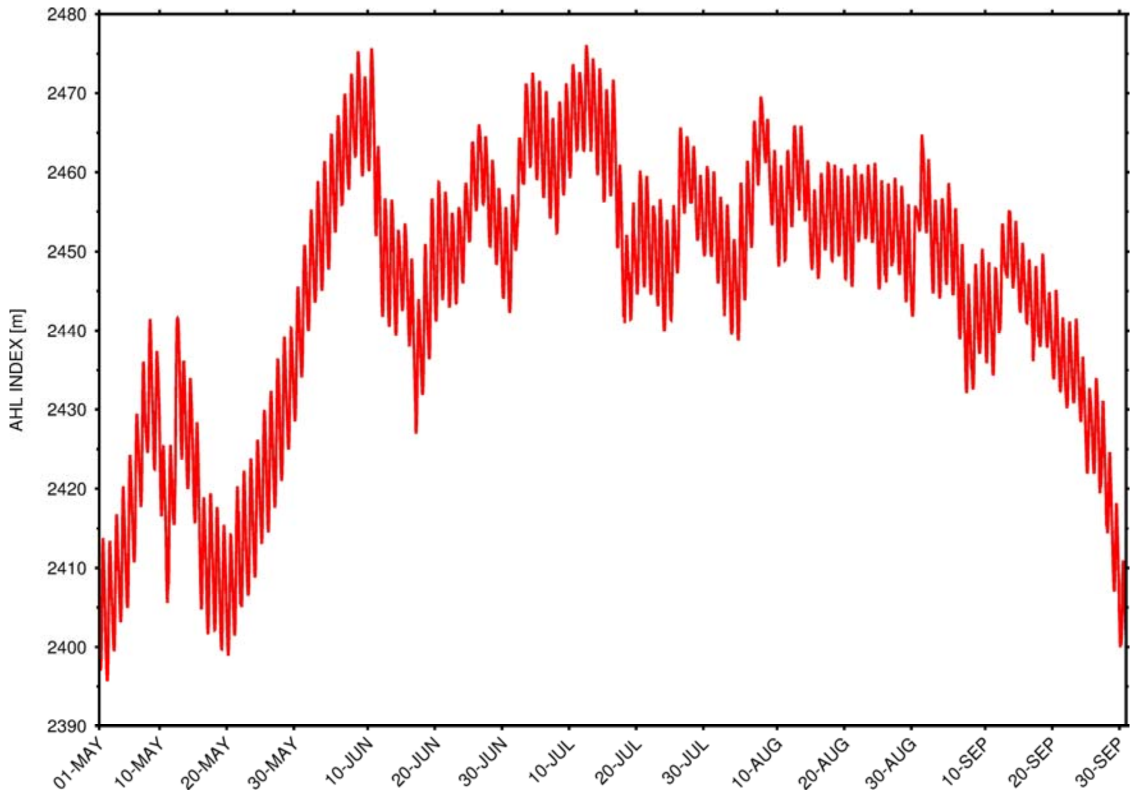

AHL INDEX [m]
2480
2470
2460
2450
2440
2430
2420
2410
2400
2390
01-MAY
10-MAY
20-MAY
30-MAY
10-JUN
20-JUN
30-JUN
10-JUL
20-JUL
30-JUL
10-AUG
20-AUG
30-AUG
10-SEP
20-SEP
30-SEP

(b)

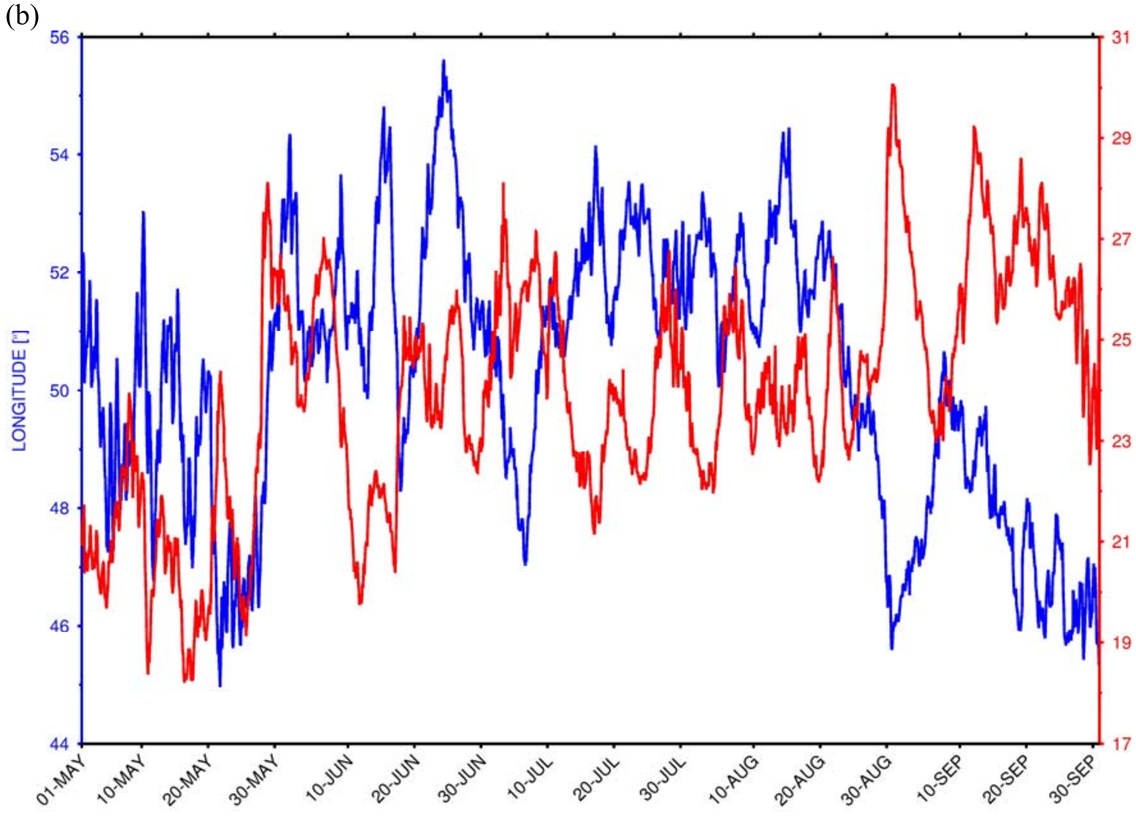

LONGITUDE [°]
LATITUDE [°]
56
54
52
50
48
46
44
31
29
27
25
23
21
19
17
01-MAY
10-MAY
20-MAY
30-MAY
10-JUN
20-JUN
30-JUN
10-JUL
20-JUL
30-JUL
10-AUG
20-AUG
30-AUG
10-SEP
20-SEP
30-SEP

(c)

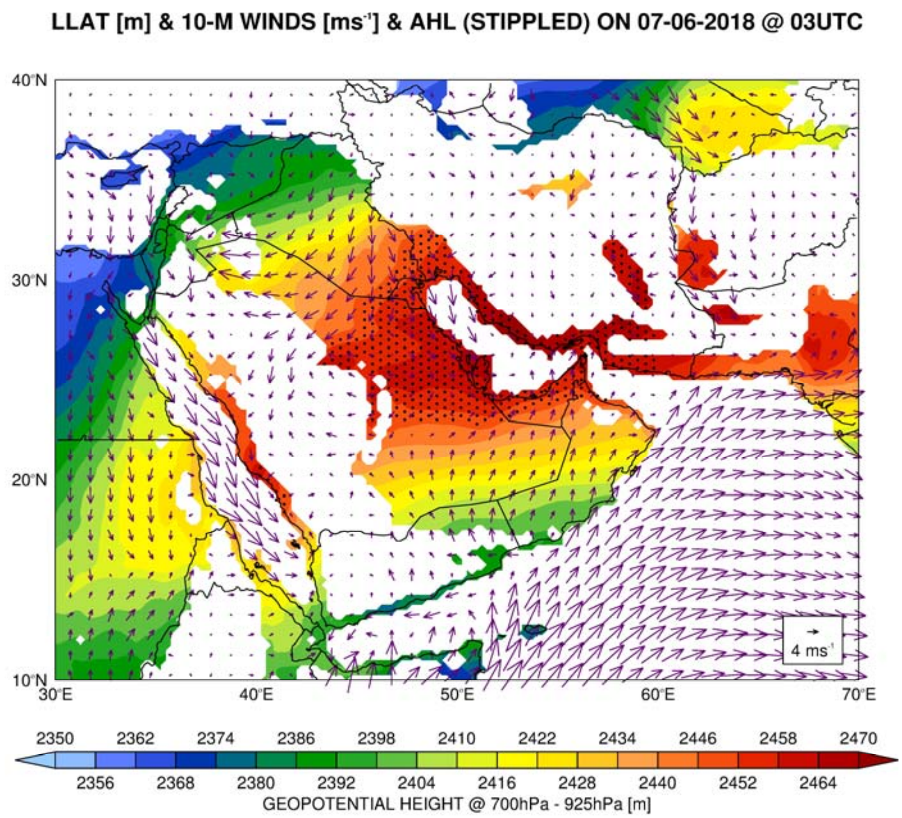
LLAT [m] & 10-M WINDS [ms-1] & AHL (STIPPLED) ON 07-06-2018 @ 03UTC
40°N
30°N
20°N
10°N
30°E
40°E
50°E
60°E
70°E
4 ms-1
2350 2362 2374 2386 2398 2410 2422 2434 2446 2458 2470
2356 2368 2380 2392 2404 2416 2428 2440 2452 2464
GEOPOTENTIAL HEIGHT @ 700hPa - 925hPa [m]

(d)

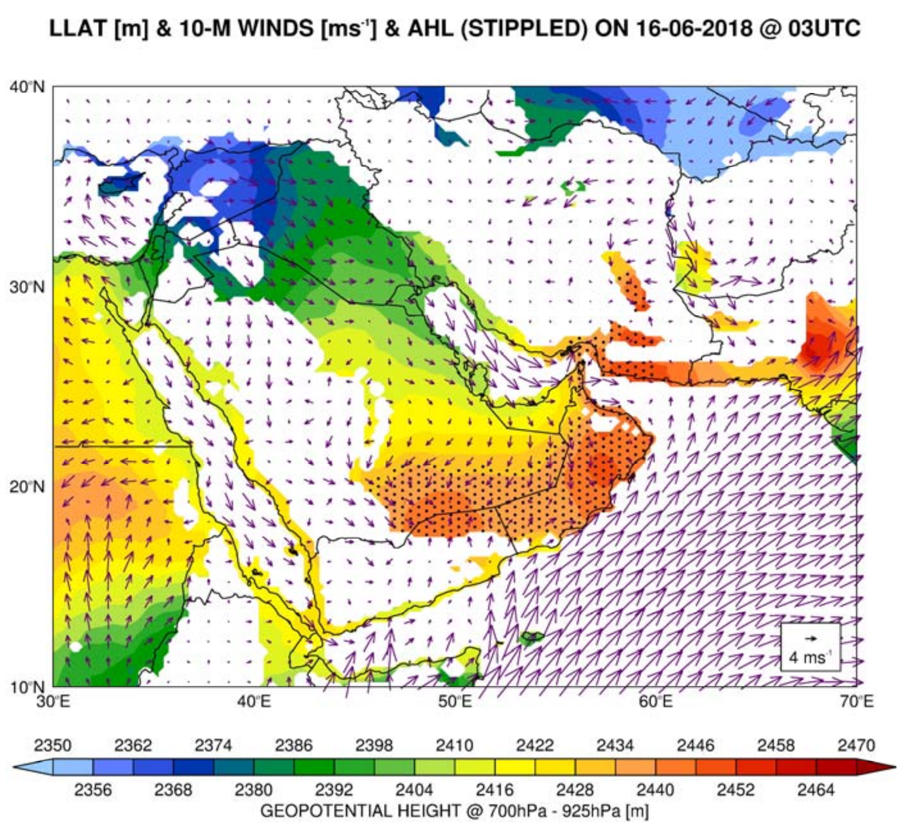
LLAT [m] & 10-M WINDS [ms-1] & AHL (STIPPLED) ON 16-06-2018 @ 03UTC
40°N
30°N
20°N
10°N
30°E
40°E
50°E
60°E
70°E
4 ms-1
2350 2362 2374 2386 2398 2410 2422 2434 2446 2458 2470
2356 2368 2380 2392 2404 2416 2428 2440 2452 2464
GEOPOTENTIAL HEIGHT @ 700hPa - 925hPa [m]

Figure 5: Hourly AHL (a) index, defined as the averaged LLAT over the AHL region, and (b) position, given by the AHL's averaged longitude (blue; °; left axis) and latitude (red; °; right axis), from May to September 2018 from ERA-5 data. (c) LLAT (m; shading), 10-meter horizontal wind vectors ($m\,s^{-1}$; arrows), and AHL (stippled region) at 03 UTC on 07 July 2018, the time around which the highest value of the AHL index for May-October 2018 is reached. The white shading denotes water bodies and areas for which the 925 hPa pressure surface is below orography. (d) is as (c) but on 16 July 2018 at 03 UTC, roughly when the lowest value of the AHL index for May-October 2018 is reached.

(a)

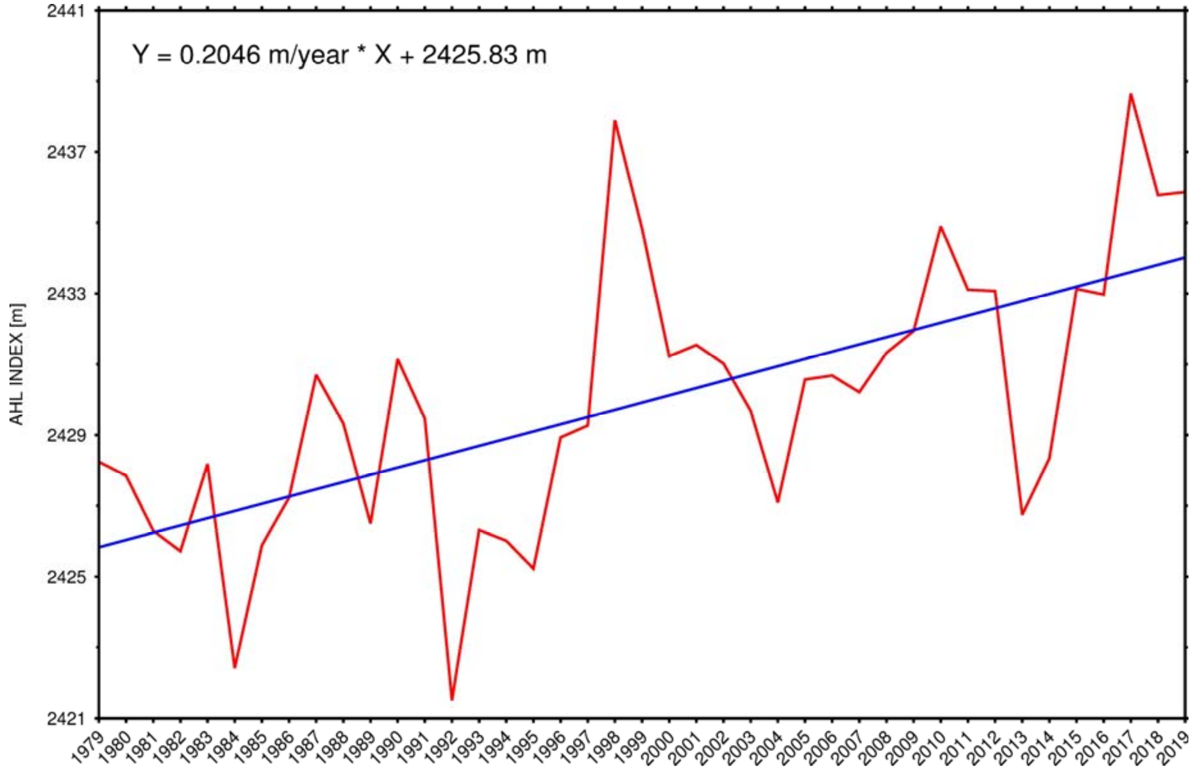
Y = 0.2046 m/year * X + 2425.83 m
AHL INDEX [m]
2441
2437
2433
2429
2425
2421
1979 1980 1981 1982 1983 1984 1985 1986 1987 1988 1989 1990 1991 1992 1993 1994 1995 1996 1997 1998 1999 2000 2001 2002 2003 2004 2005 2006 2007 2008 2009 2010 2011 2012 2013 2014 2015 2016 2017 2018 2019

(b)

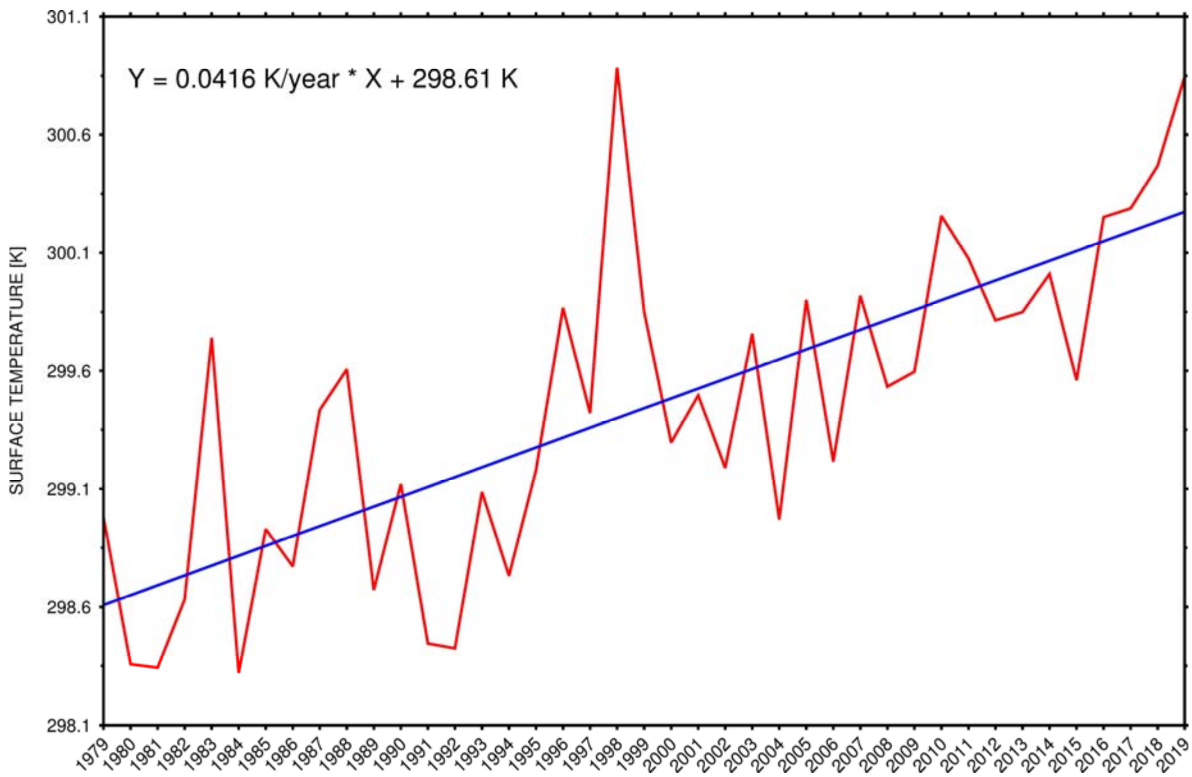
Y = 0.0416 K/year * X + 298.61 K
SURFACE TEMPERATURE [K]
301.1
300.6
300.1
299.6
299.1
298.6
298.1
1979 1980 1981 1982 1983 1984 1985 1986 1987 1988 1989 1990 1991 1992 1993 1994 1995 1996 1997 1998 1999 2000 2001 2002 2003 2004 2005 2006 2007 2008 2009 2010 2011 2012 2013 2014 2015 2016 2017 2018 2019

(c)

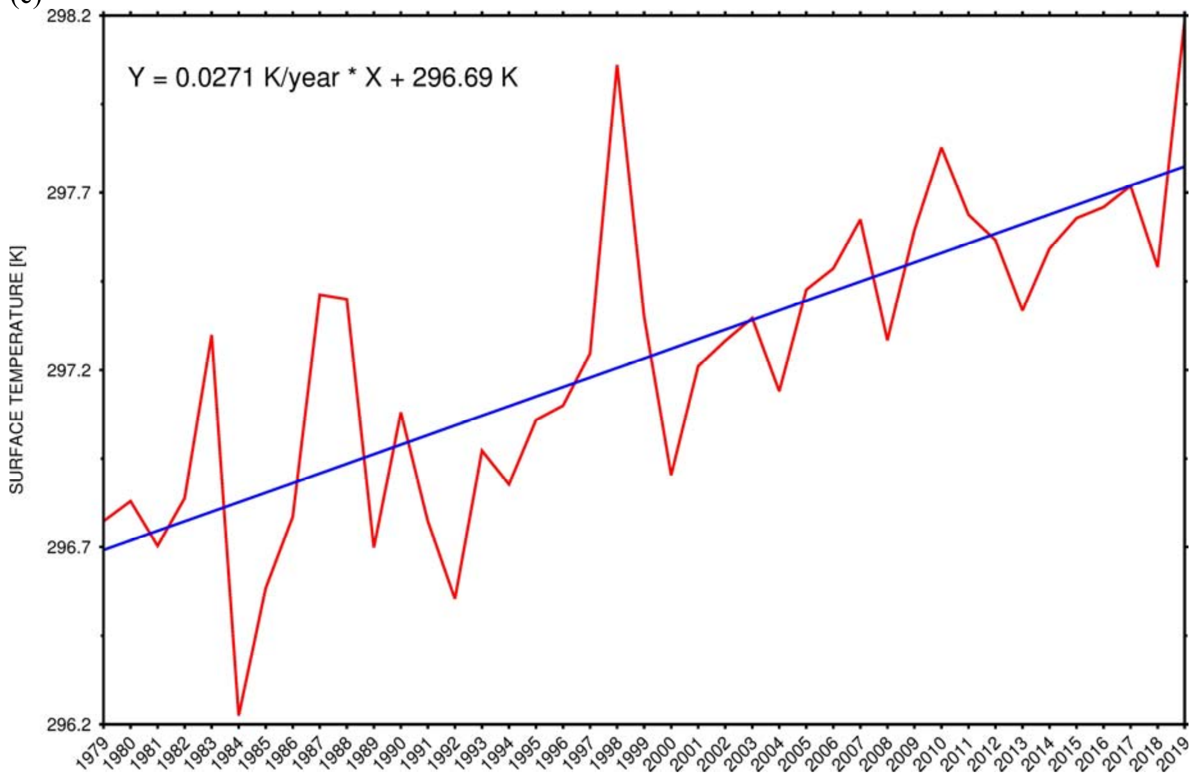

(d)

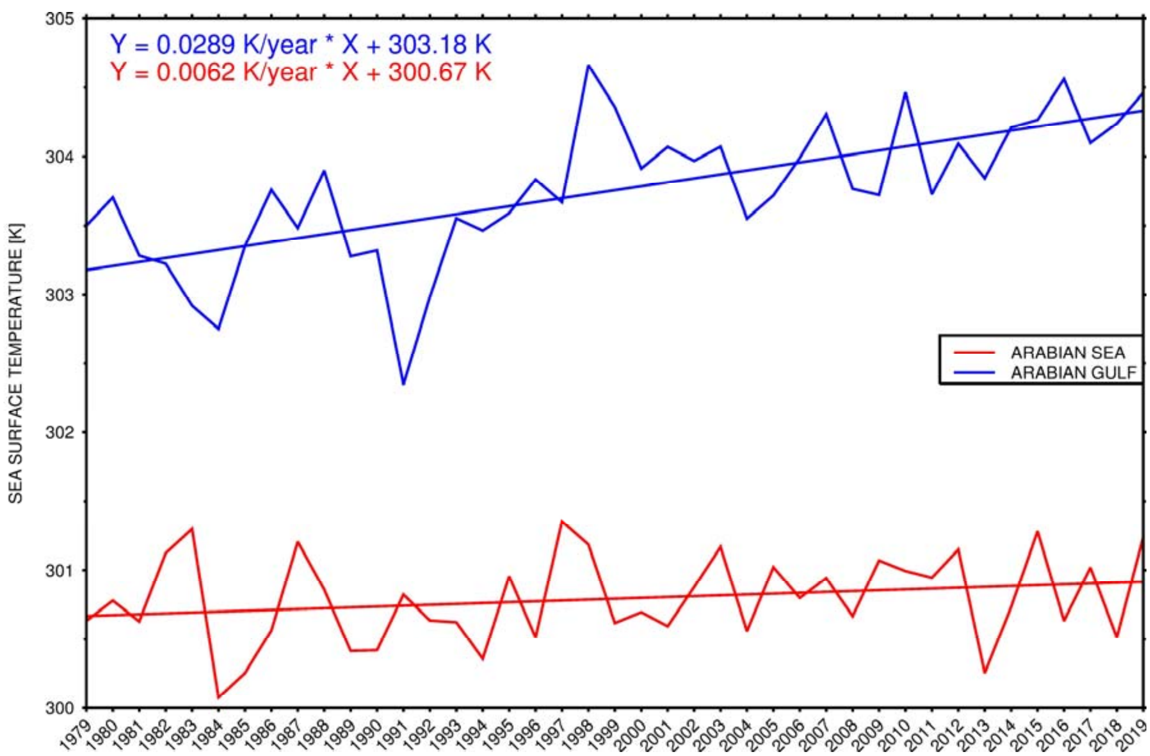

Figure 6: (a) Yearly JJAS AHL index at 03 UTC for the period 1979-2019. The blue line is the best linear fit to the data, with the equation given on the top left. (b) is as (a) but for the surface temperature (K) averaged over the AHL region, while (c) is as (b) but with the surface temperature averaged over the AHL domain (10º-35ºN and 40º-60ºE) outside the AHL region. In (d), the yearly JJAS sea surface temperatures over the Arabian Sea (red line; 5º-15ºN, 55º-70ºE) and Arabian Gulf (blue line; 20º-30ºN, 30º-55ºE) are plotted. All trends are statistically significant at the 95% confidence interval, except the one for the Arabian Sea SSTs (red line in panel (c)).

(a)

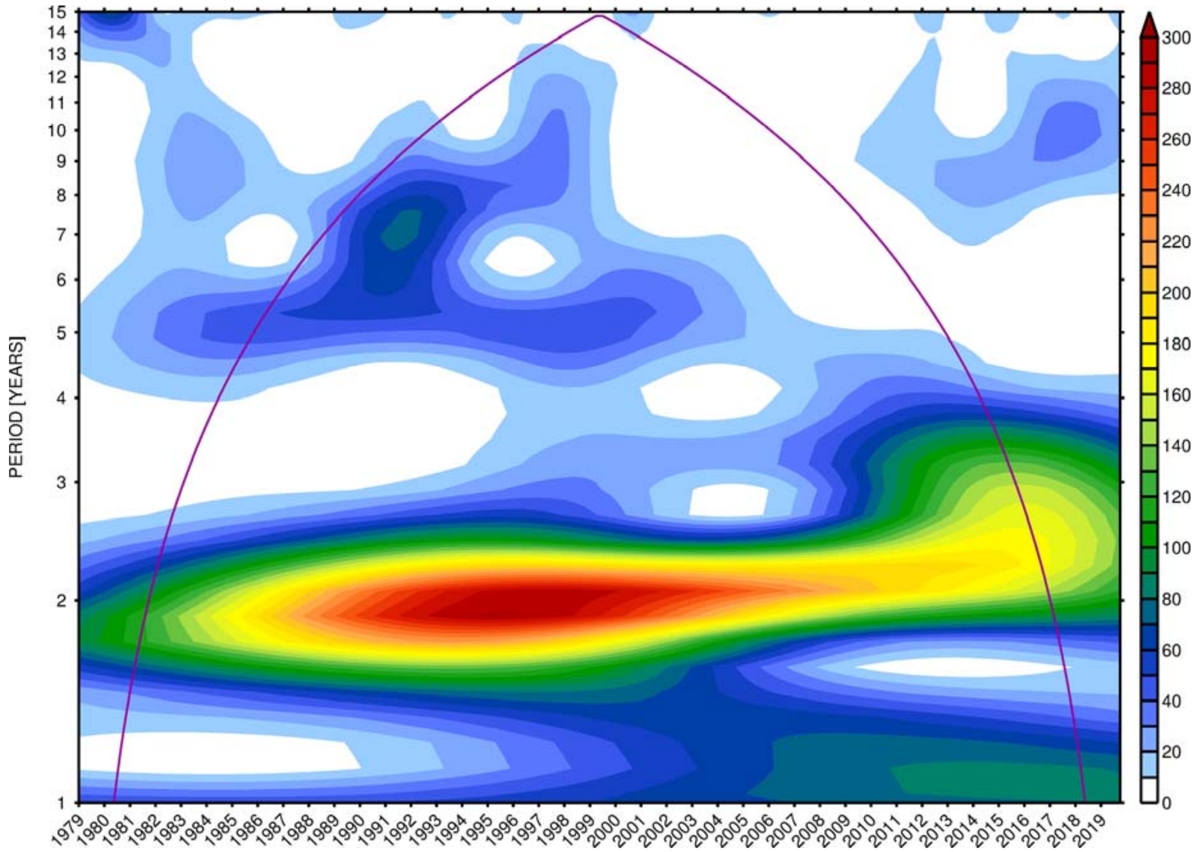
PERIOD [YEARS]
300
280
260
240
220
200
180
160
140
120
100
80
60
40
20
0

(b)

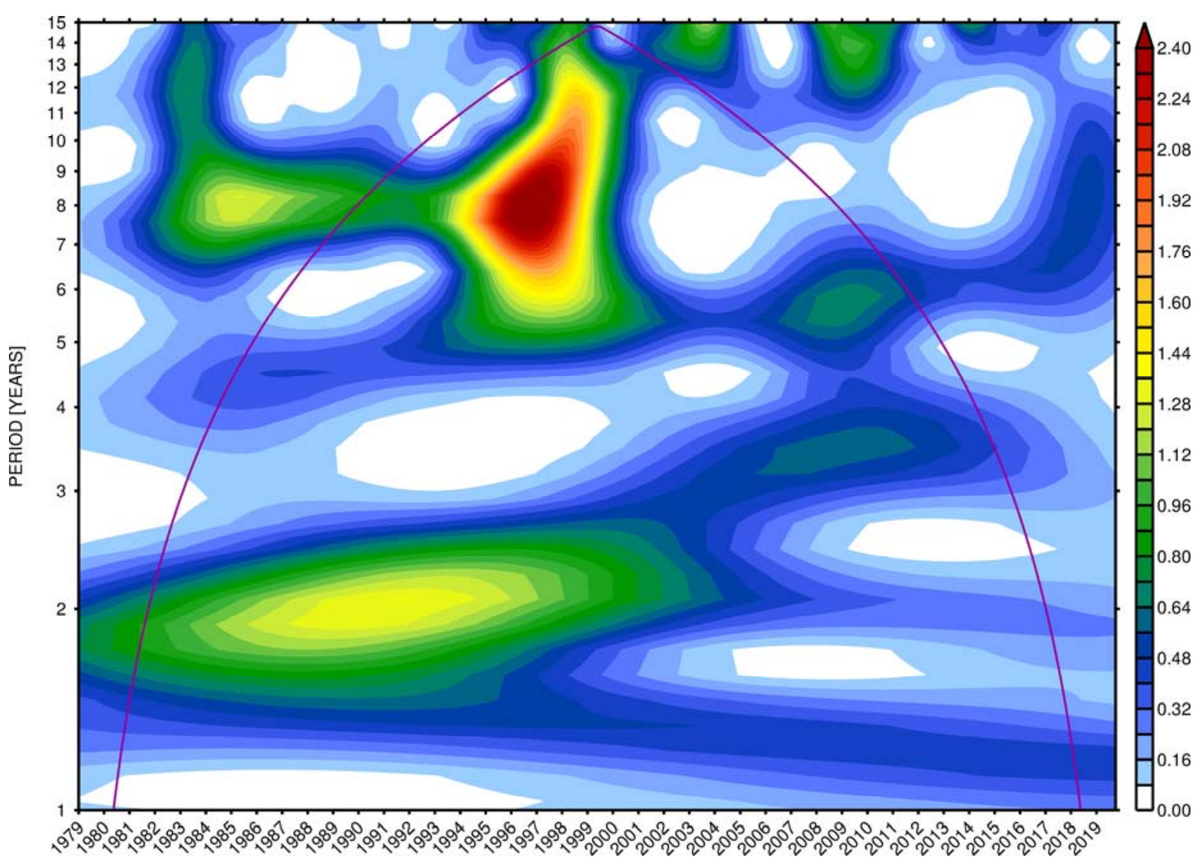
PERIOD [YEARS]
2.40
2.24
2.08
1.92
1.76
1.60
1.44
1.28
1.12
0.96
0.80
0.64
0.48
0.32
0.16
0.00

Figure 7: (a) Wavelet power spectrum, using the Morlet wavelet, of the JJAS AHL time-series (4 months for 41 years giving a total of 164 data points). (b) as (a) but for the JJAS ITD time-series. The purple line denotes the cone-of-influence, which gives the maximum period of useful information at a particular time.

(a)

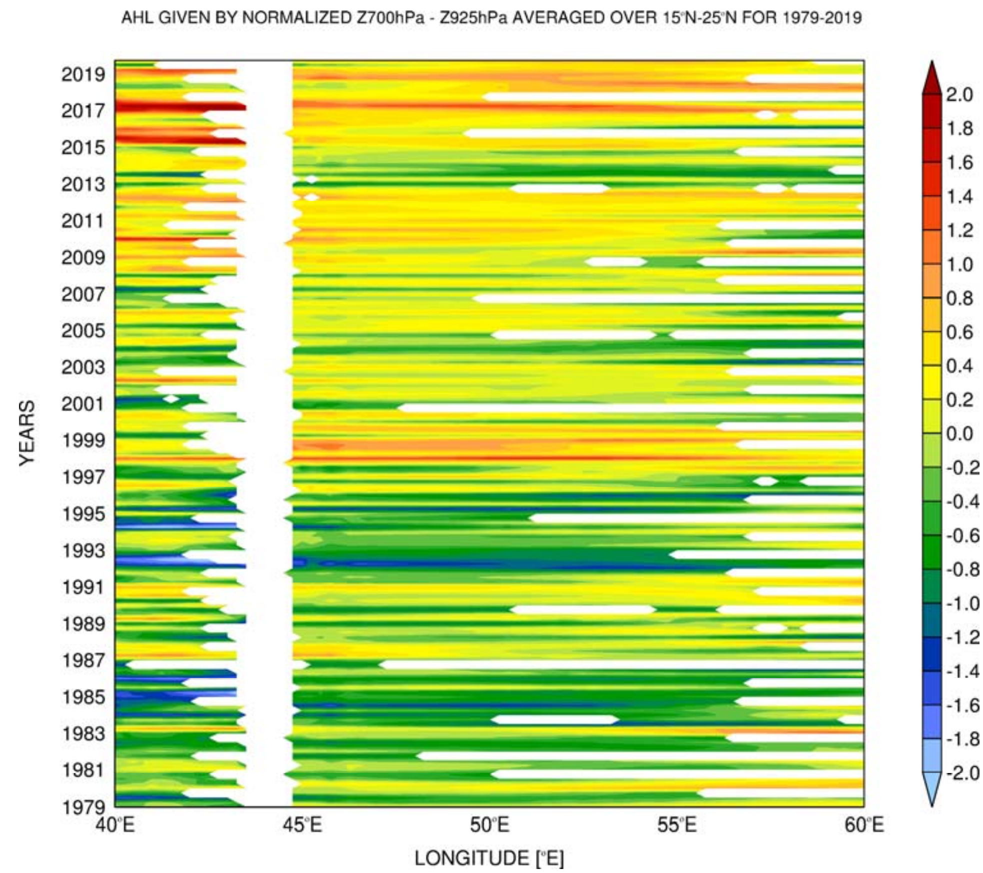
AHL GIVEN BY NORMALIZED Z700hPa - Z925hPa AVERAGED OVER 15°N-25°N FOR 1979-2019
YEARS
2019
2017
2015
2013
2011
2009
2007
2005
2003
2001
1999
1997
1995
1993
1991
1989
1987
1985
1983
1981
1979
40°E
45°E
50°E
55°E
60°E
LONGITUDE [°E]
2.0
1.8
1.6
1.4
1.2
1.0
0.8
0.6
0.4
0.2
0.0
-0.2
-0.4
-0.6
-0.8
-1.0
-1.2
-1.4
-1.6
-1.8
-2.0

(b)

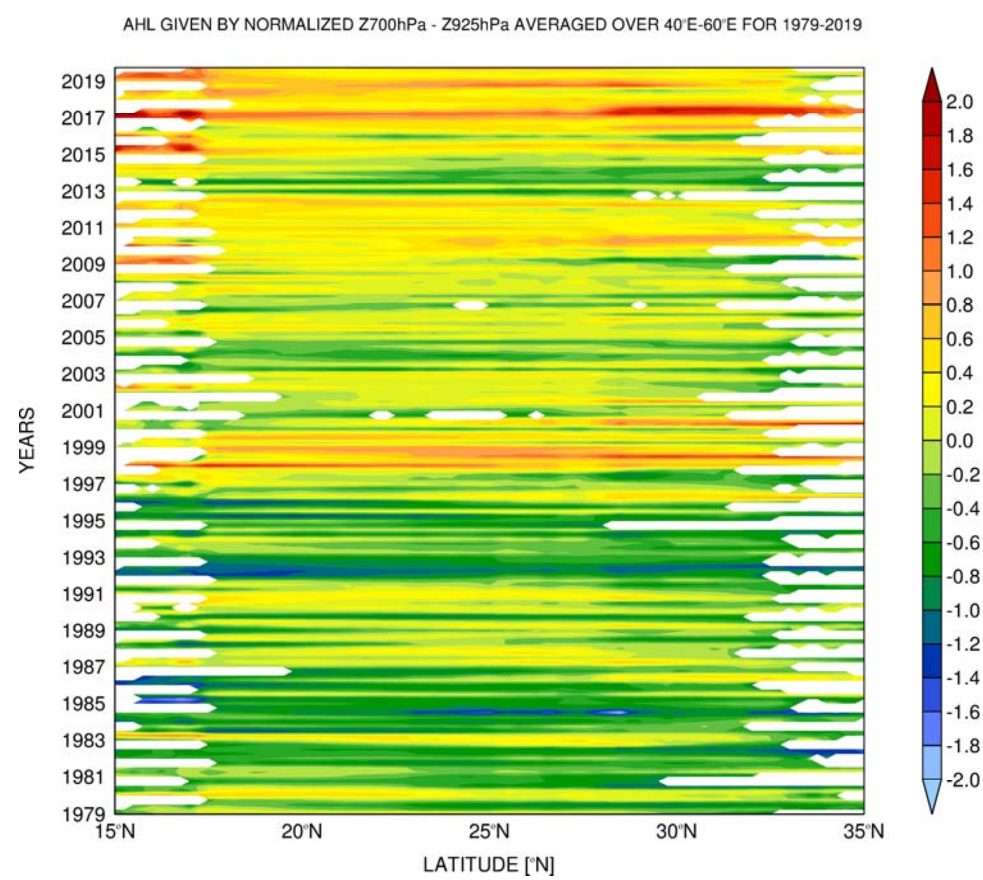
AHL GIVEN BY NORMALIZED Z700hPa - Z925hPa AVERAGED OVER 40°E-60°E FOR 1979-2019
YEARS
2019
2017
2015
2013
2011
2009
2007
2005
2003
2001
1999
1997
1995
1993
1991
1989
1987
1985
1983
1981
1979
15°N
20°N
25°N
30°N
35°N
LATITUDE [°N]
2.0
1.8
1.6
1.4
1.2
1.0
0.8
0.6
0.4
0.2
0.0
-0.2
-0.4
-0.6
-0.8
-1.0
-1.2
-1.4
-1.6
-1.8
-2.0

Figure 8: Hovmöller plots of the JJAS AHL, given by the LLAT anomalies with respect to the 1979-2019 monthly climatology normalized by its standard deviation for the 41-year period, averaged over (a) 15ºN-25ºN and (b) 40ºE-60ºE. The white shading denotes regions for which the 925 hPa pressure surface is below orography, and hence where the AHL is not defined.

(a)

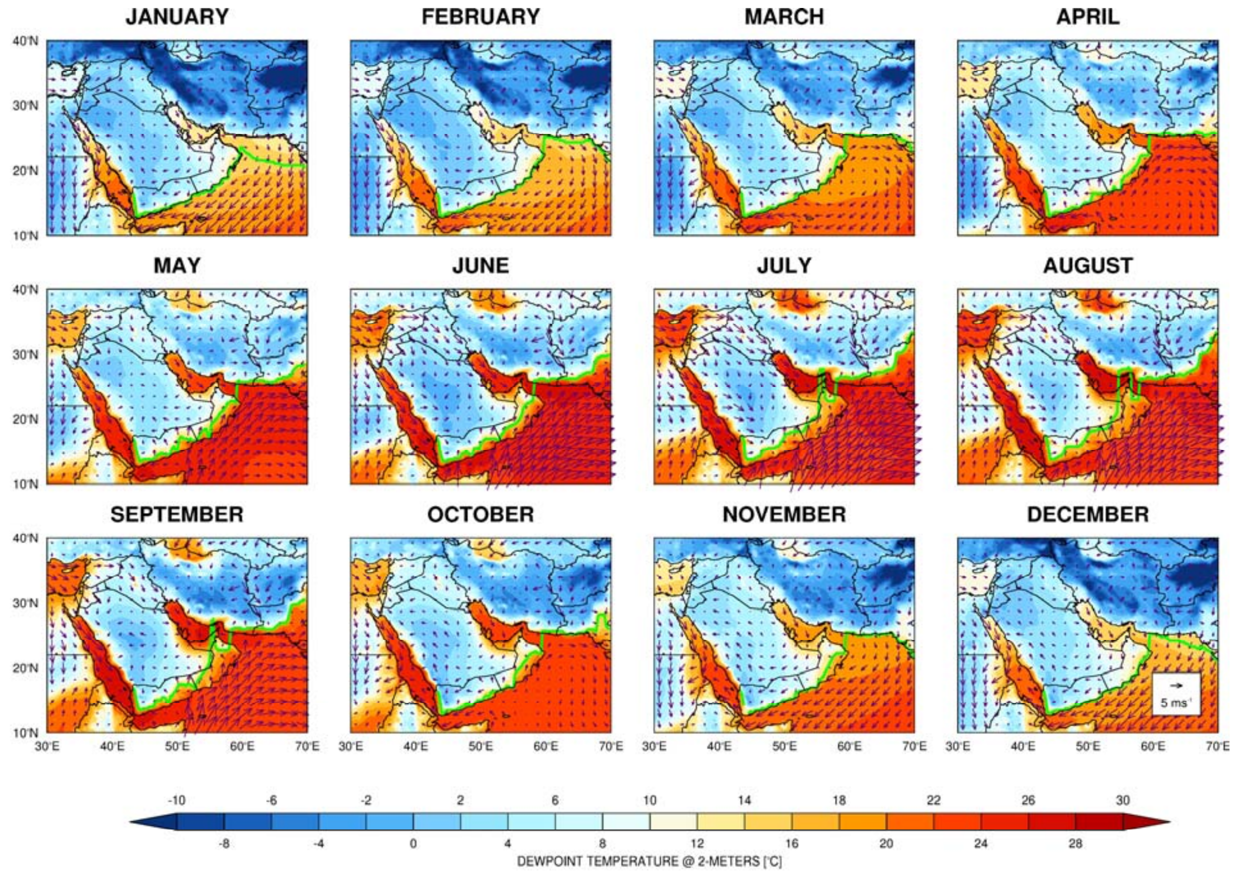

(b)

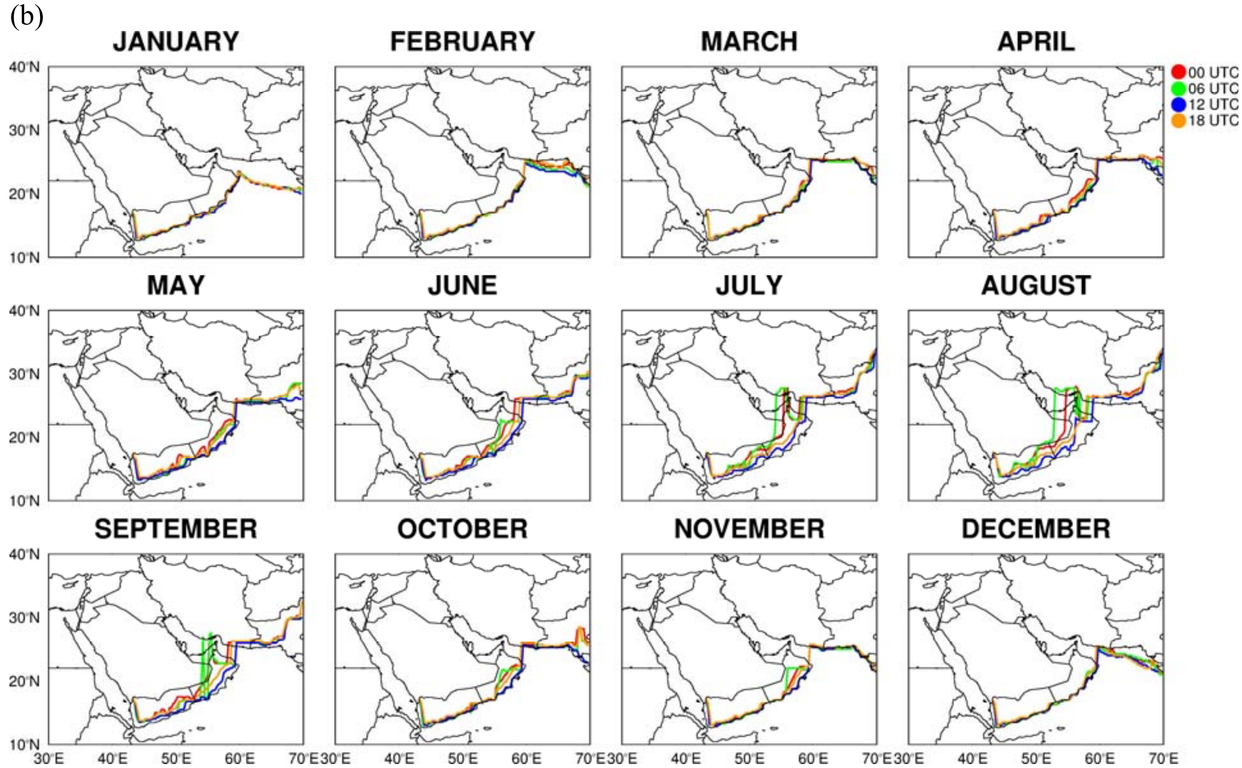

Figure 9: (a) Monthly mean 2-meter dew-point temperature (shading; ºC), 10-meter horizontal wind vector (arrows; $m\,s^{-1}$), and position of the Intertropical Discontinuity (ITD; solid green line), defined as the latitude at which the dew-point temperature at 00 UTC, decreasing northwards, is equal to 15ºC, from ERA-5 (1979-2019) data. (b) 6-hourly diurnal cycle of the ITD for each month. The ITD position at 00 UTC is shown in red, at 06 UTC in green, at 12 UTC in blue, and at 18 UTC in orange.

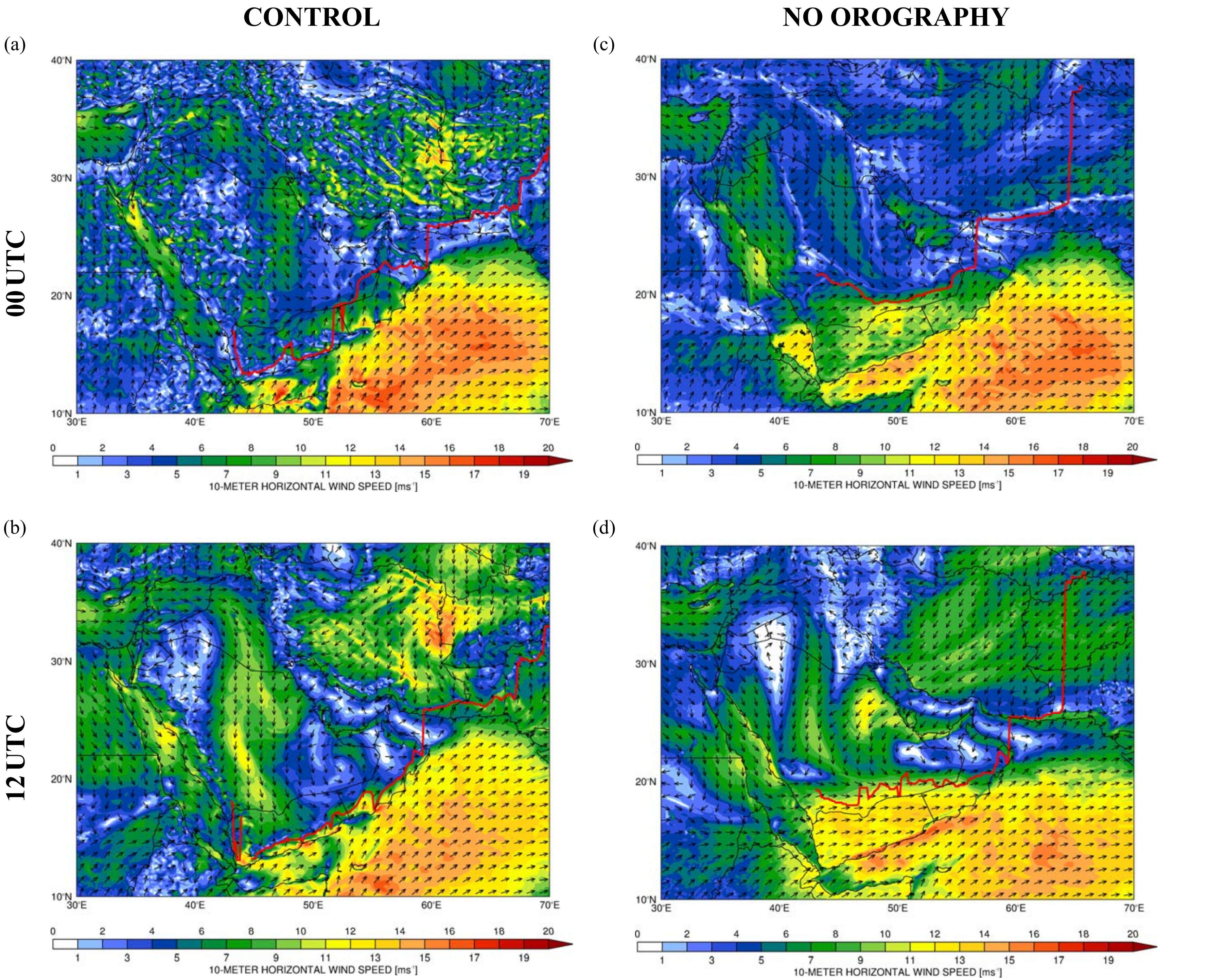

Figure 10: WRF-predicted 10-meter horizontal wind (the shading gives the magnitude in m s^{-1}, and the black arrows give the direction) and ITD (solid red line) on 11 June 2018 at (a) 00 and (b) 12 UTC. (c)-(d) are as (a)-(b) but for a semi-idealised experiment in which all the orography was removed.

(a)

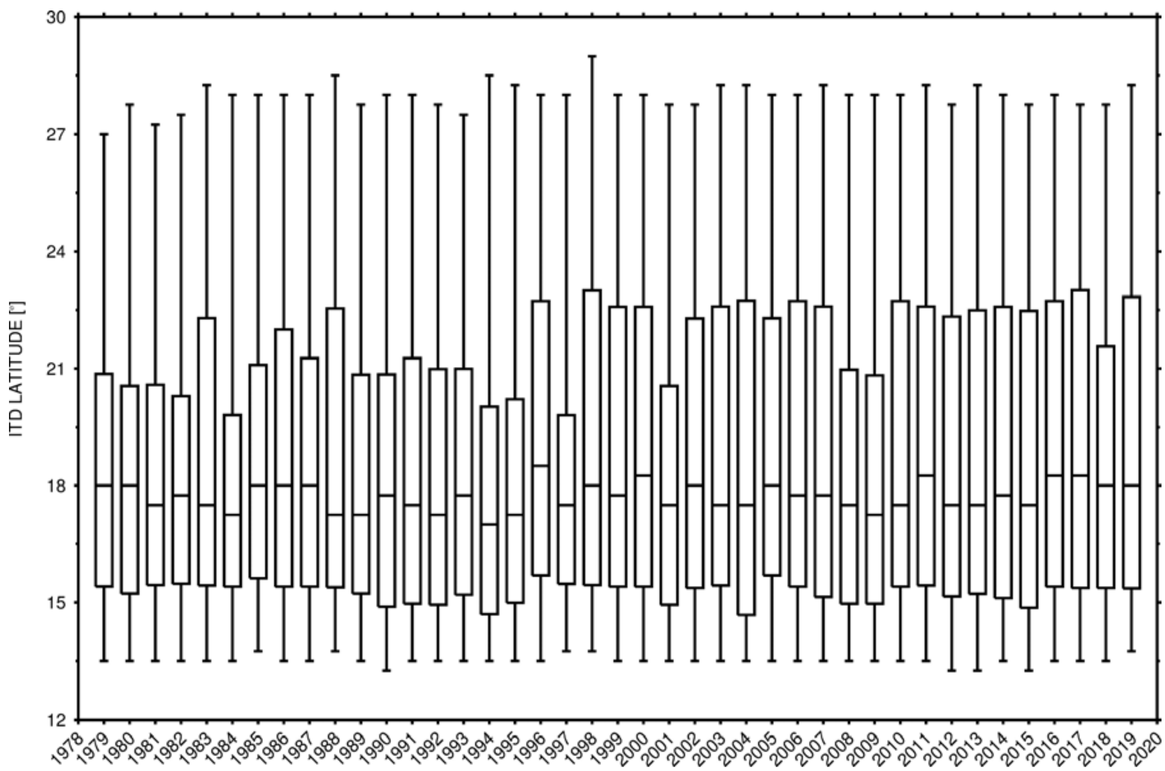

(b)

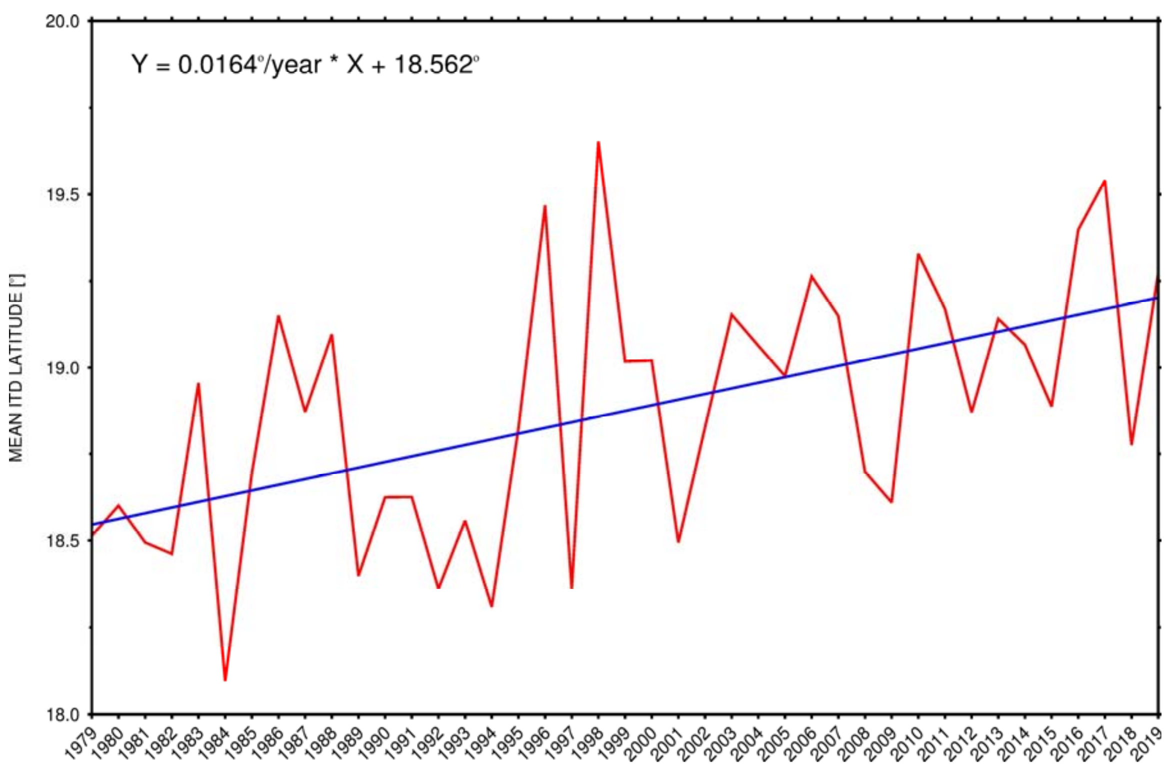

Figure 11: (a) Box plot showing the minimum, first quartile, median, third quartile, and maximum of the latitudinal position of the ITD (°) for JJAS in the longitude range 40º-60ºE for each year from 1979 to 2019. (b) Monthly time-series of the ITD index (°), averaged over JJAS of each year, from 1979 to 2019. The blue line is the best linear fit to the data, with the equation given on the top left.

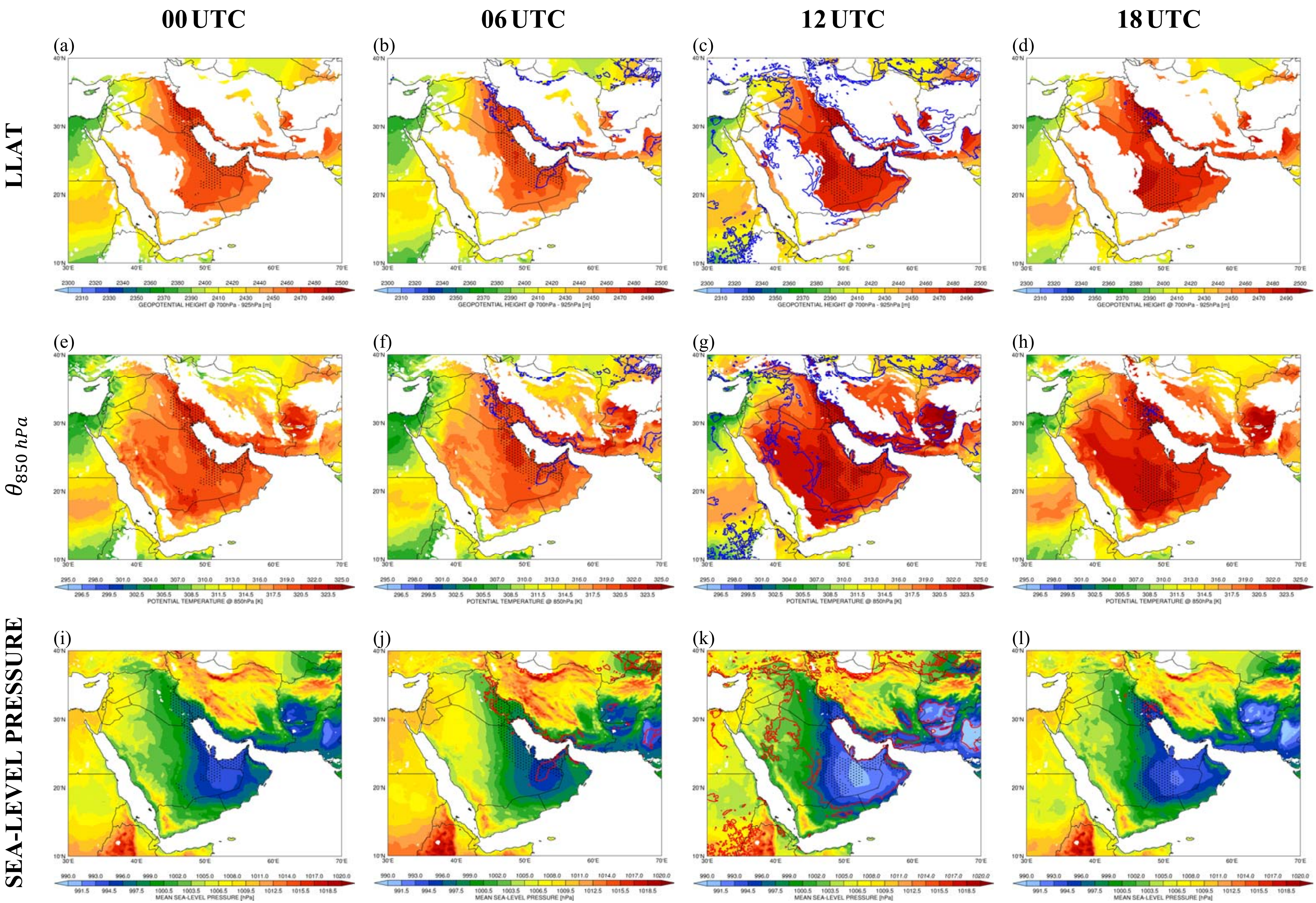
00 UTC
06 UTC
12 UTC
18 UTC
LLAT
$\theta_{850\ hPa}$
SEA-LEVEL PRESSURE
(a)
(b)
(c)
(d)
(e)
(f)
(g)
(h)
(i)
(j)
(k)
(l)
GEOPOTENTIAL HEIGHT @ 700hPa - 925hPa [m]
POTENTIAL TEMPERATURE @ 850hPa [K]
MEAN SEA-LEVEL PRESSURE [hPa]

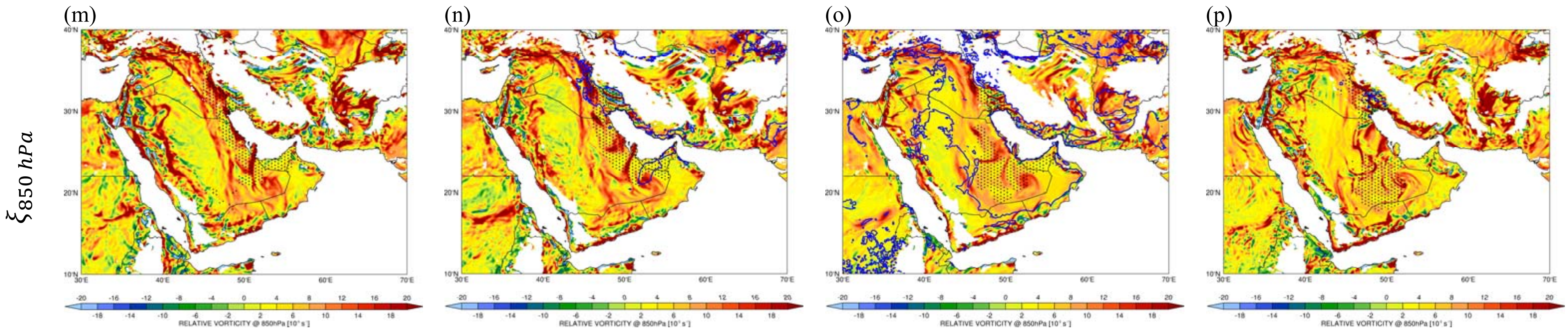

Figure S1: As Figure 2 but for the WRF simulation.